Topology optimization for dual-flow heat exchangers of moderate conductive material within a narrow design domain: Numerical and experimental investigations

Ahmad Fawaz, Yuchao Hua, Steven Le Corre, Yilin Fan, Lingai Luo, Gwenaël Biotteau

Topology optimization for dual-flow heat exchangers of moderate conductive material within a narrow design domain: Numerical and experimental investigations

Ahmad Fawaz, Yuchao Hua*, Steven Le Corre, Yilin Fan, Lingai Luo†, Gwenaël Biotteau

Nantes Université, CNRS, Laboratoire de thermique et énergie de Nantes, LTeN, UMR6607, F-44000 Nantes, France

*Corresponding author: Email: yuchao.hua@univ-nantes.fr

†Corresponding author: Email: lingai.luo@univ-nantes.fr

Abstract

Heat exchangers (HXs) play a critical role in various energy systems, which can largely influence their overall efficiency. Most recently, the interest in the topology optimization (TO) of heat transfer, which can derive innovative thermal designs, is growing rapidly. Therefore, the present work investigates the utility of the density-based TO for dual-flow HX unit of moderate conductive material (Stainless Steel (SS)) and narrow design domain, along with CFD (computational fluid dynamics) and experimental verifications. The objective of the TO is to maximize the heat exchange rate, while a pressure drop constraint is imposed on the HX's flow channels to avoid the blocking issues. An in-depth investigation is conducted to study the effect of various TO's input parameters on the derived topology. The obtained results reveal that the TO-derived design is mainly featured by the solid allocation in proximity to the insulation walls but not at the interface wall that separates hot and cold fluids (where heat is exchanged). Furthermore, high fidelity CFD simulations along with experimental approaches (including Infrared thermography) are employed to validate the TO's design methodology and the numerical model. The experimental and numerical results present good agreement between each other, demonstrating the thermo-hydraulic performance superiority of the TO-acquired design compared to the benchmark case with an intensification in the exchanged heat up to 15% under the same pumping power. Lastly, a physical interpretation is delivered to analyze the underlying physics behind the TO-acquired topologies.

Keywords: Topology optimization, heat exchangers, Fins design, Computational fluid dynamics, Infrared thermography.

Nomenclature

Latin letters

$\boldsymbol{v}$	Velocity (m/s)
P	Pressure (Pa)
$f(\gamma)$	Brinkman Coefficient
S_f	Volumetric heat capacity (J.m^{-3}.K^{-1})
C_s	Volumetric heat capacity ratio
k_f	Fluid thermal conductivity (W.m^{-1}.K^{-1})
T	Temperature (K)
C_k	Thermal conductivity ratio
k_s	Solid thermal conductivity (W.m^{-1}.K^{-1})
$\boldsymbol{n}$	Normal vector
v_{in}	Inlet velocity (m.s^{-1})
T_{in}	Fluid inlet temperature (K)
T_{out}	Fluid outlet temperature (K)
q	Penalization coefficient
p	Penalty factor
b	Convexity parameter
$\dot{m}$	Mass flow rate (kg.s^{-1})
Q	Heat transfer rate (W)
v_{fs}	Solid fraction
Da	Darcy Number
Re	Reynolds Number
Pe	Peclet Number
A	Heat transfer area (m^2)
h	Heat transfer coefficient (W.m^{-2}.K^{-1})
$\overline{Re_{cold}}$	Mean *Re* of the cold fluid
$\overline{Re_{hot}}$	Mean *Re* of the hot fluid
D_h	Hydraulic diameter (m)
R	Filter radius (m)
f	Friction coefficient
l	Length of heat exchanger (m)
E	Energy (W)
c_p	Specific heat (J.kg^{-1}.K^{-1})
R_{th}	Thermal resistance (K.W^{-1})
Bi	Biot number

Greek symbols

γ	Densities (Design Variables)
ρ_f	Fluid density (kg.m^{-3})
μ	Fluid viscosity (Pa.s)
γ_i	Initial design variable
α	Inverse permeability
α_{max}	Maximum inverse permeability
ΔP	Pressure drop (Pa)
∇T	Temperature gradient
ΔT_m	Logarithmic mean temperature difference (K)
γ_β	Projection point
γ_f	Filtered Design Variables
γ_p	Projected Design Variables

Abbreviations

TO	Topology optimization
CFD	Computational fluid dynamics
HX	Heat exchanger
FEM	Finite element method
MMA	Method of moving asymptotes
GCMMA	Globally convergent MMA
SNOPT	Sparse nonlinear optimizer
IOPOPT	Interior point optimizer
SIMPLE	Semi implicit method for pressure linked equations
SS	Stainless Steel

1. Introduction

Heat exchangers (HXs) are thermal devices that exchange heat between different mediums (e.g., fluid-fluid, fluid-solid) with or without direct contact, for generally realizing various fundamental operations like cooling, drying, and heating, etc [1]–[3]. They play a crucial role in many industrial processes by allowing the thermal energy transfer efficiently, which make them one of the most impactful thermal devices on the overall efficiency of the energy systems. Therefore, how to increase the HX's performance has been for a long time a hot topic for engineers and researchers [4]–[6]. For improving the performance of HXs, many research have been conducted within the context of heat transfer enhancement. Passive techniques such of using extended surfaces as fins has been well-demonstrated as one of the most effective techniques in increasing heat transfer rates by disrupting established boundary layer, but at the cost of significantly increased pumping power needed [7]. A prevalent practice involves the placement of fins on the HX's interfacial wall proximal to heat source or where heat exchange occurs, with the intention of extending the heat surface area and then intensifying the exchanged heat [8]–[10]. In this context, high-conductive materials such as aluminum or copper are typically employed aiming to mitigate the conduction resistance [11].

With the development of computer technologies, optimal designs of HX structure become possible with the assistance of numerical simulation and various optimization algorithms [12]. In the literature, three main optimization techniques are employed to optimize the configuration of the HXs for achieving improved performances, namely size, shape and topology optimization. The size/shape optimization holds relatively small number of design variables, and is generally constrained by the pre-defined shape of the targeted elements [13]–[15]. By contrast, the topology optimization (TO) can have the maximum number of design variables, and thus maximized performance can be theoretically achieved without any geometry presetting [12]. With the rapid rise of TO in the recent years, it is anticipated that TO may became a leading technique for thermal designs [16]–[21].

According to the literature, several important research gaps can be identified as follow:

1. Currently, the TO is mainly conducted on one-flow HXs (more than 90% of the existing research in the literature) under the specific name as heat sinks [22]–[24], according to the statistics in our review paper [12] that covers most of the relevant publications in the past two decades. Nevertheless, in real practice, HXs frequently work with at least two flows.
2. The majority of the design problems employed in TO of HXs literature [12] generally introduce wide (Aspect ratio=Length/width of the design domain < 2) design domains that allows the structure to freely evolve during the TO process [25]–[27]. However, this may contradict with some actual applications where the fluid area is considerably restricted as in compact HXs.
3. Few researchers (about 18%) in the TO of HXs literature [12] fabricated the TO-derived structures and the majority (about 82%) limit their research to the numerical approaches by performing CFD analysis to evaluate the performances of the TO-derived structures. As for the TO of dual-flow HXs specifically, our statistics indicate that no existing research have experimentally tested the TO-derived structures [12]. Nevertheless, the experimental approach is considered as an indispensable step to validate the numerical models.
4. Lack of physical interpretation of the optimized structures, as it is always needed for better understanding and possible generalization of the results.

Considering the aforementioned issues, the present work employs the density-based TO method to optimize the thermo-hydraulic performance of a dual-flow HX unit

with narrow design domain (length/width = 18). The TO-derived design is featured by a novel arrangement of fins that can maximize the heat transfer rate between two fluids separated by a moderate conductive material (SS). This original fin structure, always persists under varied TO input parameters, has then been verified with a series of CFD simulations, experimental approaches and physical interpretations.

The present paper is decomposed as follows: Section 2 provides the problem formulation and the detailed methodology of the TO. Section 3 presents the acquired topologies with an in-depth investigation on the influence of TO's input parameters. Section 4 introduces the employed CFD analysis and experimental approaches to validate the design methodology. Section 5 presents the comparison the thermo-hydraulic performance evaluated numerically and experimentally for all HX units. Section 6 summarizes the main conclusions and perspectives.

2. Topology optimization

2.1 Problem formulation

2.1.1 Design problem and conjugate heat transfer physics

Due to the significant computational time of the topology optimization (TO), it is challenging to be directly conducted on a 3D industrial HX. Therefore, simplifications are necessary in order to facilitate the feasibility of the TO process. Accordingly, a simplified 2D HX unit is introduced as depicted in figure 1. The design problem is a 2D counter-flow HX unit that permits the exchange of heat between two fluids (cold and hot fluids) through a thin solid wall with 1 mm of thickness. The flow channels of the cold and hot fluids have an equal width of 9 mm and the overall dimensions of the HX unit are 162 mm (wide) and 21 mm (height).

It is noteworthy to mention that the TO's design domain (where the TO act) are the HX's flow channels, while the top, middle and upper solid plates are excluded from the TO process.

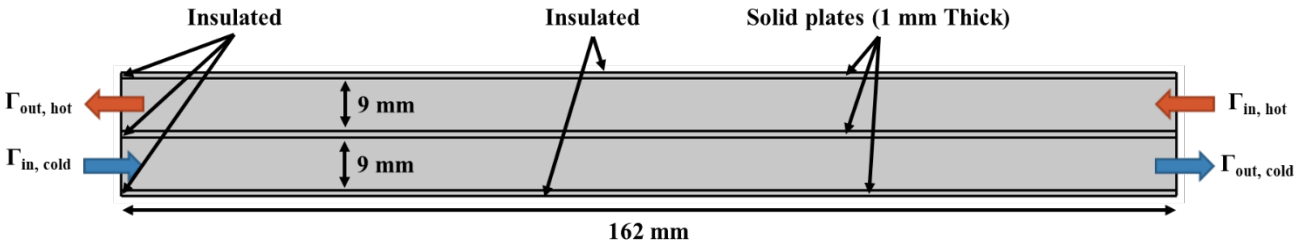

Figure 1: TO's design problem with the corresponding dimensions in mm.

The conjugate heat transfer physics in HXs combines the fluid dynamics and heat transfer models. The incompressible and steady-state fluid flow in the HX is modelled using the continuity and momentum equations, given as below:

$$\nabla . \boldsymbol{v} = 0$$
$$\rho_f (\boldsymbol{v} . \nabla)\boldsymbol{v} = -\nabla P + \mu . \nabla^2 v - \boldsymbol{f}(\gamma) \quad (1)$$

where $\boldsymbol{v}$ is the velocity (m.s^{-1}), P the pressure (Pa), μ the fluid dynamic viscosity (Pa.s), ρ_f the fluid density (kg.m^{-3}), and γ is the TO's design variables. In the density-based TO, the momentum equation needs to be modified by adding a Brinkman friction $\boldsymbol{f}$ coefficient as defined in Eq. (2), to model the fluid flow in the design domain treated as a porous medium:

$$\boldsymbol{f}(\gamma) = \alpha(\gamma)\boldsymbol{v} \quad (2)$$

where α is the inverse permeability that must be interpolated between the solid and fluid phases to define the optimized flow path (the detailed interpolation function equations will be introduced in the TO section).

The heat transfer will be studied in the solids that are dominated by conduction and in the fluids that are dominated by convection. The steady-state energy equation is utilized to model the heat transfer of the HX.

$$S(\gamma)\boldsymbol{v} . \nabla T - \nabla . (k(\gamma)\nabla T) = 0 \quad (3)$$

where T is the temperature (K), $S(\gamma)$is the volumetric heat capacity interpolation function (J.m^{-3}.K^{-1}) and $k(\gamma)$ is the thermal conductivity interpolation function (W.m^{-}

^{1}.K^{-1}). The detailed interpolation function equations will be provided in the following section (section 2.2).

2.1.2 Boundary Conditions

As illustrated in Fig.1, a set of Dirichlet boundary conditions are imposed at the inlet of each fluid by setting a uniform velocity and temperature profiles as follow:

$$\begin{aligned} -\boldsymbol{v}.\boldsymbol{n} = v_{in} &\iff \text{on } \Gamma_{in,cold} \text{ and } \Gamma_{in,hot} \\ T = T_{f,cold} &\iff \text{on } \Gamma_{in,cold} \\ T = T_{f,hot} &\iff \text{on } \Gamma_{in,hot} \end{aligned} \tag{4}$$

where $T_{f,cold}$, $T_{f,hot}$ are the inlet temperatures of the cold and hot fluids, respectively, and $\boldsymbol{n}$ is the normal vector to the corresponding boundary outwardly oriented to the design domain. Similarly, a uniform pressure and outflow conditions are set at the outlet boundaries of fluid flows.

$$\begin{aligned} P = 0 &\iff \text{on } \Gamma_{out,cold} \text{ and } \Gamma_{out,hot} \\ -\boldsymbol{n}.\nabla T = 0 &\iff \text{on } \Gamma_{out,cold} \text{ and } \Gamma_{out,hot} \end{aligned} \tag{5}$$

Moreover, an adiabatic condition is imposed on the top and bottom walls, as well as the extreme ends of HX unit, as illustrated in Figure 1.

2.2 TO methodology

2.2.1 Design Parametrization

The density-based parametrization is based on representing the design domain (fluid channels in the present case) by densities or porosities (design variables) to parametrize the fluid and solid phases. In this study, the initial density distribution has been set to an intermediate design variable, γ_i =0.5, i.e., each mesh element is composed initially of a porous medium that contains 50% fluid and 50% solid. Throughout the TO procedure, the density values (γ) can exhibit a continuous variation ranging from 0 (fluid) to 1 (solid). As for the interpolation scheme, the inverse permeability is interpolated between the solid and fluid phases using the following

formula [25]:

$$\alpha(\gamma) = \alpha_{max} * q * \frac{\gamma}{q + 1 - \gamma} \tag{6}$$

where α_{max} is the maximum impermeability value and q is a penalization coefficient. The maximum impermeability is computed using the following formula [28]:

$$\alpha_{max} = \frac{\mu}{Da.{D_h}^2} \tag{7}$$

where *Da* is the dimensionless Darcy number that represents the permeability effect of the porous medium [29]. Concerning the thermo-physical properties interpolation, the RAMP (rational approximation of material properties) interpolation function is used to interpolate the value of the thermal conductivity and the volumetric heat capacity between the solid and fluid phases. The aim behind is founded in the demonstrated capability of the RAMP function to penalize a broader range of intermediate design variables when compared with the classical SIMP (Solid Isotropic Material with Penalization) function [30]. Therefore, the thermal conductivity $k(\gamma)$ and volumetric heat capacity $S(\gamma)$ interpolation functions are expressed respectively as follows [31]:

$$\begin{aligned} k(\gamma) &= k_f \frac{(1-\gamma)(C_k(1+b)-1)+1}{C_k(1+(b(1-\gamma))} \\ S(\gamma) &= S_f \frac{(1-\gamma)(C_s(1+b)-1)+1}{C_s(1+(b(1-\gamma))} \end{aligned} \tag{8}$$

where b is the convexity parameter of the function, S_f is the volumetric heat capacity of the fluid phase ($J.m^{-3}.K^{-1}$), k_f is the thermal conductivity of the fluid phase ($W.m^{-1}.K^{-1}$), C_k and C_s are the thermal conductivity ratio and the volumetric heat capacity ratio, respectively, between the fluid and solid phases.

2.2.2 Filter and projection

During the topology generation, filters and projections are necessary to avoid the numerical instabilities (checkerboard, mesh dependency, local optimum, etc.) caused by the ill-posedness of the TO problems [32]. For the filtering technique, the Helmholtz PDE filter [33] is adopted to obtain an averaged filtered design variables γ_f:

$$\gamma_f = R^2\nabla^2\gamma_f + \gamma \tag{9}$$

where R is the filter radius which is considered as the mesh element size in the current study. After the filtering process, an intermediate density area near the solid-fluid interface is generated. In order to reduce it, the filtered design variables are projected using the smooth Heaviside hyperbolic tangent projection [34]:

$$\gamma_p = \frac{\tanh\left(\beta\left(\gamma_f - \gamma_\beta\right)\right) + \tanh\left(\beta\gamma_\beta\right)}{\tanh\left(\beta\left(1 - \gamma_\beta\right)\right) + \tanh\left(\beta\gamma_\beta\right)} \tag{10}$$

where γ_p is the projected design variable, β is the projection slope and γ_β is the projection point.

2.2.3 Optimization problem formulation

In this research, the primary objective of the TO is to maximize the exchanged heat (Q) between the cold and hot fluids inside the HX which can be expressed as [35]:

$$Q = \int_{out} E\, d\Gamma - \int_{in} E\, d\Gamma = Sf\left(\int_{out} \boldsymbol{v}.T\, d\Gamma - \int_{in} \boldsymbol{v}.T\, d\Gamma\right) \tag{11}$$

where E is the energy (W). To constraint the non-linear problem, a set of constraints have been imposed. First, a constraint is imposed on the maximal pressure drop inside the flow channels to avoid the blocking issues caused by elevating the value of the maximum impermeability. Moreover, the continuous design variable field γ is bounded between 0 (fluid) and 1 (solid). Additionally, the governing equations presented in Eqs. (1) & (4) should be also set as a constraint to ensure that their residuals will be zero in each iteration of the optimization process. Eventually, a solid fraction is imposed to constraint the amount of solid generated in the flow channels. Thus, the TO's mathematical problem can be summarized as follows:

$$
\begin{aligned}
&Find\ \gamma \\
&Max\ Q\ (Eq.12) \\
&s.t \begin{cases} 0 \le \gamma \le 1 \\ \dfrac{\int_{\Gamma_{in,cold}} P}{n * \Delta P_{bareHX,cold}} - 1 < 0 \\ \dfrac{\int_{\Gamma_{in,hot}} P}{n * \Delta P_{bareHX,hot}} - 1 < 0 \\ \dfrac{\int_{\Omega} \gamma d\Omega}{v_{fs}} - 1 \le 0 \\ Eqs.(1),(4) \end{cases}
\end{aligned} \tag{12}
$$

where v_{fs} is the maximum allowed solid volume fraction and Ω is the design domain. $\Delta P_{bareHX,cold}$ and $\Delta P_{bareHX,hot}$ are the pressure drop in the cold and hot channels of the bare HX (empty channels) respectively, and n is the maximal allowable pressure drop ratio.

2.2.4 COMSOL implementation

The implementation of the TO models for the 2D counter-flow HX unit is carried out using the Finite Element Method (FEM)-based commercial software COMSOL 6.0. The CFD Module of COMSOL is employed to address the fluid problem (Eq. 1) with a first-order discretization scheme for velocity and pressure. Simultaneously, the Heat Transfer Module is utilized to solve the energy equation (Eq. 4), employing a first-order discretization scheme for the temperature field. As for the Helmholtz PDE filter, a linear discretization scheme is used and the filter radius is set twice of the maximum element size. The purpose of setting the filter radius twice the element size rather than the maximum element size is to increase minimum length scale in the TO, thereby avoiding the appearance of very small solid structures in the flow channels. Such small structures do not significantly influence the HX's performance and are challenging to manufacture. The TO's design domain is discretized using a triangular mesh consisting of 160,000 elements. The governing equations are subjected to the streamline stabilization scheme, while the upwind stabilization scheme is omitted. The direct solver PARDISO, integrated into COMSOL, is utilized for solving the discretized governing equation.

Furthermore, segregated solver steps are utilized to address the fluid problem, thermal problem, and filter PDE. Gradient optimization is conducted through the utilization of the Optimization Module in COMSOL. This module solves the adjoint problem to furnish the sensitivities of both objective and constraint functions for the globally convergent method of moving asymptotes (GCMMA) [36], serving as the optimizer for iteratively updating the topology throughout the optimization process.

A conservative continuation strategy is applied on the penalization coefficients (q and b) of the interpolation functions and the projection slope (β), to attenuate a possible convergence to a local optimum. The proposed continuation scheme is composed of ten steps as shown in Table 1. For the first steps, low parameters values are set to stabilize the TO process and guarantee better sensitivity scaling by giving the optimizer some freedom. Then, the parameters values are slowly increased in the last steps to acquire more precise physical models by penalizing the intermediate densities and sharping the interfaces. This continuation strategy leads to better performance and gives more stability to the topology generation process than starting with the final parameters values which often leads to fast convergence to a local optimum in such a non-convex optimization problem [37]. It is noteworthy that a less conservative continuation strategy involving a reduction in both the number of continuation steps and model evaluations is feasible, but with an elevated risk of converging towards a poor local optimum.

Table 1: Continuation scheme for penalization and projection coefficients

Step	1	2	3	4	5	6	7	8	9	10
q	0.01	0.01	0.01	0.03	0.03	0.08	0.1	0.1	0.1	0.1
b	0.1	0.1	0.1	5	5	20	50	50	50	50
β	1	1	1	2	3	4	5	6	8	8

2.2.5 TO setting parameters

The values of the TO's input parameters are summarized in Table 2. First, the

Reynolds number (Re) is computed according to the inlet boundaries for simplicity using the following equation:

$$Re = \frac{\rho_f \, v_{in} D_h}{\mu} \tag{13}$$

where v_{in} is the inlet velocity (m.s^{-1}). The hydraulic diameter (D_h) is assumed to be double of the height for an infinite wide channel [24],[38]. Since the acquired topology has been reported to be strongly influenced by the input parameters of the TO [39], a thorough examination of the effect of these parameters on the resulting topology will be extensively discussed in the results section. Furthermore, the projection point γ_β of the hyperbolic projection process is set to 0.5. The working fluid employed in the TO is water, while the solid material is SS. The properties of both water and SS are assumed to be temperature independent, as outlined in Table 3.

Table 2: TO input parameters

Parameter	Value
Re	50-150
D_h [mm]	18
Da	10^{-5}
v_{fs}	(5% - 30%)
γ_β	0.5
n	3-10
C_k	0.04
C_s	1.72
S_f [J.m^{-3}.K^{-1}]	4.18e6
R [mm]	0.5

Table 3: Material properties used in the TO [40]

Parameter	water	SS

$k\ [W.m^{-1}.K^{-1}]$	0.61	15
$\rho\ [kg.m^{-3}]$	1000	7800
$C_p\ [J.kg^{-1}.K^{-1}]$	4182	468
$\mu\ [Pa.s]$	1e-3	-

3. TO-results and discussion

3.1 Effect of Reynolds number (Re)

Figure 2 shows the optimized topologies acquired at three Reynolds numbers of 50,100 and 150. The TO-derived topology is distinctly characterized by the strategic allocation of the solid fins on the upper and lower plates, proximate to the insulation of the HX unit, rather than at the middle wall that separates the hot and cold fluids. Moreover, a conspicuous characteristic includes a distinct inclination in the geometry of the fins directed towards the central plate of the HX unit. As the *Re*

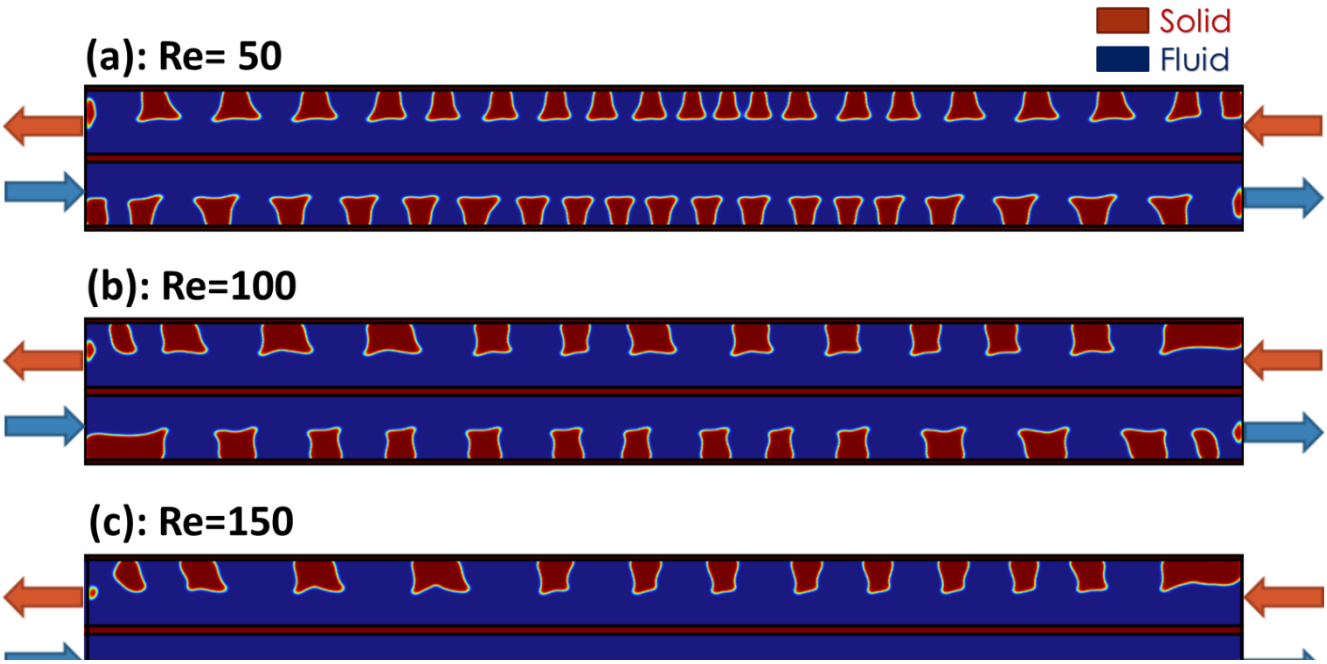

Figure 2: Optimized topology at **(a):** *Re*=50, **(b):** *Re*=100, **(c):** *Re*=150 under n=5 and $v_{fs} = 0.2$.

increases from 50 to 150, the number of fins generated within the cold and hot flow channels decreases simultaneously. The topology obtained at Re = 50 has 42 fins as seen in Fig.2a, whereas the topologies acquired at Re = 100 and Re = 150, each features 28 fins as illustrated in Figures 2b and 2c, all under the same imposed solid fraction (20% solid, 80% fluid). As for the fin's height, the three acquired topologies exhibit identical average fin height of 4.1 mm, which can be attributed to the imposition of the same maximal admissible pressure (n=5) inside the flow channels of all topologies presented in Fig.2. Furthermore, a notable change in the geometry and distribution of the fins is evident, as illustrated in Figure 2, which will underscore the pronounced sensitivity of TO-derived topology to the variation of the Re.

3.2 Effect of the maximal imposed pressure drop intensity

Within this subsection, an examination is conducted to investigate the impact of the maximum admissible pressure drop ($n \times \Delta P_{bareHX}$) within the flow channels on the acquired topologies. As the n value increases from 3 to 10, the average height of the generated fins increases accordingly from 3.5 mm at n=3 to 4.1 mm at n=5 and 5.5 mm at n=10, while having the same imposed solid fraction (20% solid and 80% fluid) as seen in Fig. 3. With the increase of the fin's height, the flow channels become narrower, leading to a local increase in the velocity of the fluid close to the middle wall and therefore intensifying the exchanged heat (objective function). For more quantitative comparisons, the number of fins differ in three acquired topologies as illustrated by Fig.3, with 34 fins, 28 fins and 26 fins in the TO-derived designs at n=3, n=5 and n=10, respectively. This investigation strongly evidences the crucial necessity of incorporating a pressure drop constraint in the TO process, in order to prevent potential blocking issues within the flow channels of the HX.

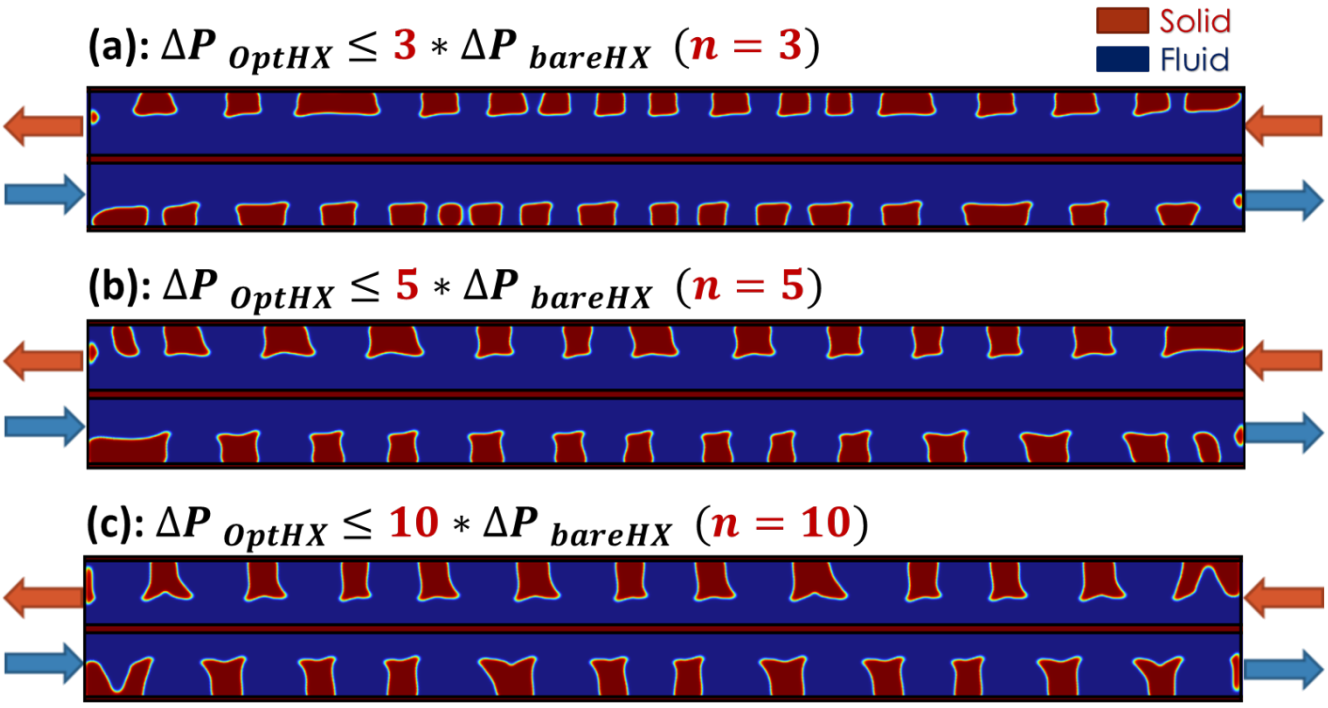

Figure 3: TO-derived HXs at **(a)**: n=3, **(b)**: n=5, **(c)**: n=10 under Re=100 and $v_{fs} = 0.2$.

3.3 Effect of initial density distribution

Given the paramount significance of the initial guess in the optimization process,

particularly in gradient optimization, various initial distributions of densities are tested, as delineated in Figure 4. The visual representation demonstrates that the acquired topologies have similar solid allocations, with a slight difference in the distribution of fins in the flow channels of the HX. Moreover, a negligible difference in the final optimized value of the objective function for the different TO-derived structures has been noted. This underscores the robustness of the employed methodology and the major reason behind this marginal difference may be addressed to the incorporation of a conservative continuation scheme, which will decrease the possibility of converging to a poor local optimum. For a quantitative comparison among the six acquired topologies, the average fin height remains consistent at 4.1 mm. Regarding the number of fins in the flow channels, the three acquired topologies with a uniform initial density distribution, illustrated in Figures 4a, 4b, and 4c, each consists of 28 fins. In contrast, the three acquired topologies with an initial discrete density distribution (only solid and fluid phases), presented in Figures 4d, 4e, and 4f, each contains 26 fins, while the solid fraction (20% solid and 80% fluid) is maintained the same in all six TO-derived structures.

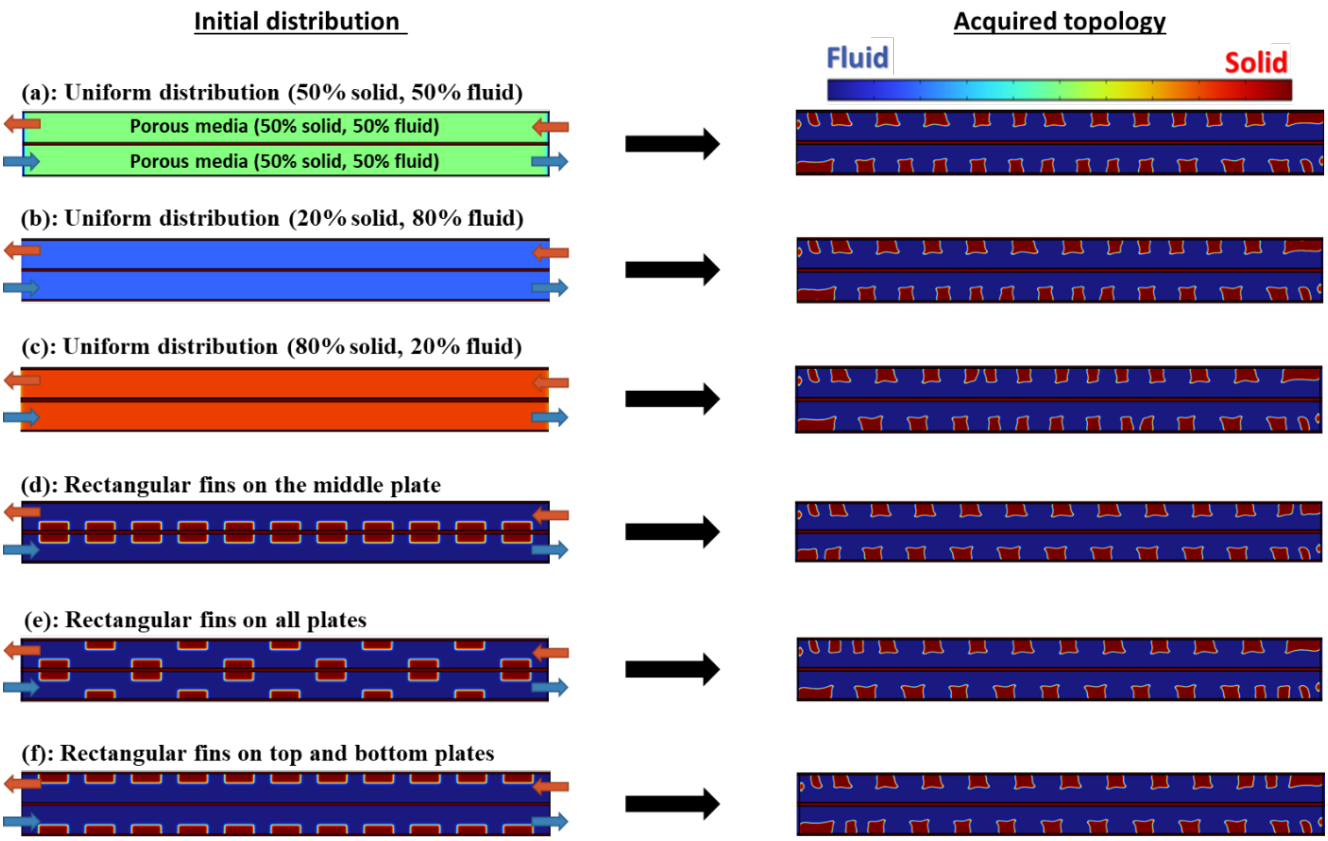

Figure 4: Acquired topologies using different initial distribution of the densities at *Re*=100, *n*=5 and $v_{fs} = 0.2$.

3.4 Effect of final solid fraction

The optimization process incorporates a constraint on the amount of generated solid. The impact of varying the imposed percentage of generated solids on the resulting topology is examined in this subsection. Figure 5 clearly demonstrates that the width of the generated solids increases by increasing the imposed solid fraction while maintaining consistent solid allocation on the upper and lower plates of the HX unit. Moreover, the three acquired topologies under different imposed solid fraction of 5%, 20% and 30%, exhibit 28 fins, 28 fins and 26 fins, respectively, although the average height of the generated fins in the HX's flow channels for the three presented cases is almost identical, measuring 4.1 mm. Furthermore, it is noteworthy to mention that the maximum height of the generated fins in the HX's flow channels for the three presented cases is almost identical. This can be explained by the analogous imposed maximal

pressure drop (n=5) in the flow channels for the three acquired topologies. Additionally, the appropriate solid fraction should be determined based on the user's requirements or the designer's experience. Increasing the solid fraction results in higher material usage, which increases material costs and can also lead to higher pressure losses. Therefore, a tradeoff between enhancing heat transfer and minimizing hydraulic losses must be considered when selecting the solid fraction value. Besides, the appropriately selected solid fraction value should be identical with that of the reference case to ensure a fair comparison.

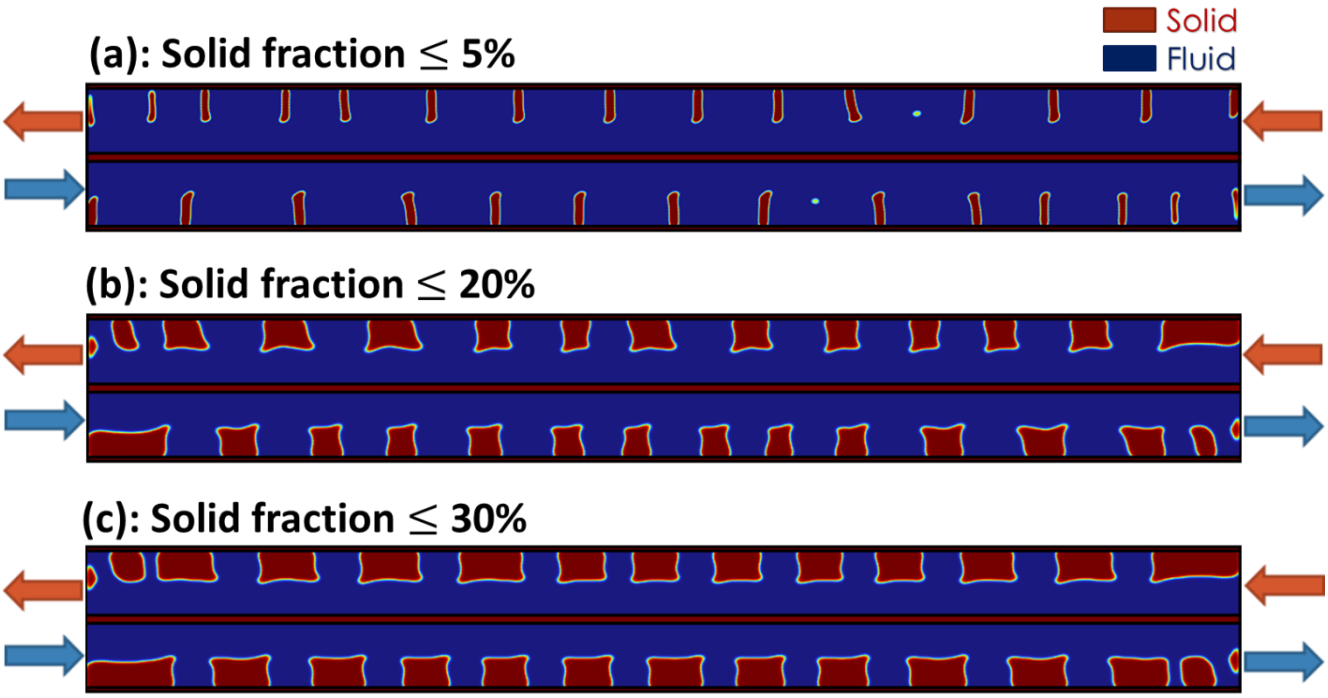

Figure 5: Optimized topologies at different imposed solid fraction under Re=100, n=5.

3.5 Effect of different gradient optimizers

In the literature, several gradient optimizers are implemented in the TO for HXs for the purpose of finding the optimum value of a specific objective under several constraints [12]. However, the effect of different gradient optimizers employed in the TO on the acquired topology has not yet been investigated so far [12]. Therefore, three gradient optimizers, including GCMMA, SNOPT (Sparse nonlinear optimizer) [41] and IOPOPT (Interior point optimizer) [42] are utilized and compared in this study, under the same input parameters, objective function and constraints. The three investigated gradient optimizers hold different mathematical background and thus the distinct

approaches. Detailed explanations behind their mathematical background are beyond the scoop of this paper and can be found in the mentioned references. As depicted by Figure 6, a remarkable difference has been observed in the TO-acquired topologies using different gradient optimizers, mainly by the distinct shape and number of the generated fins. Additionally, a negligible difference (about 0.1 %) in the optimum achieved value of the objective function has been observed. This reflects the robustness of the density-based TO method in achieving the maximized performance.

For more comparison between the three optimizers, the computational times for the TO using the MMA (13 hours 59 minutes), SNOPT (14 hours 5 minutes), and IPOPT (13 hours 48 minutes) optimizers are comparable, with no significant differences observed. From a numerical perspective, the MMA optimizer has more numerical stability compared to the two other optimizers, as it defines two moving asymptotes (upper and lower) that varies in each iteration of the optimization process to maintain the numerical stability and avoid any divergence problem even when handling various constraints. Lastly, according to our statistics [12], the MMA optimizer is the most widely used optimizer in the TO literature, highlighting its robustness and compatibility with the TO method.

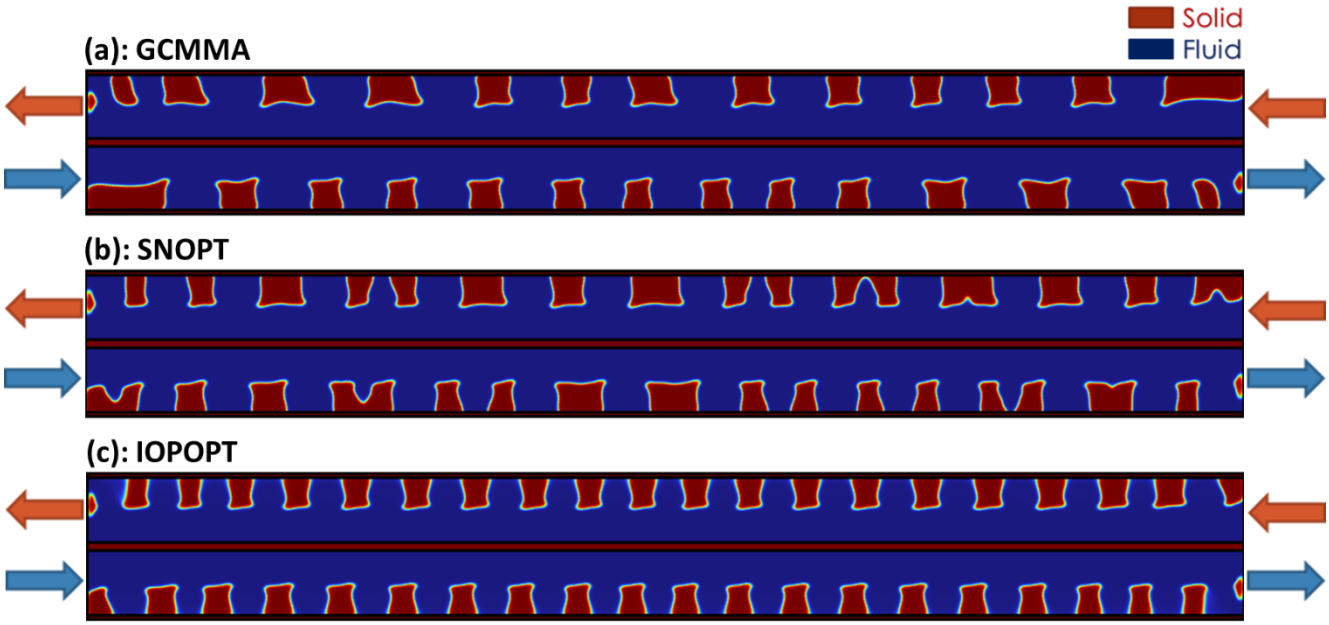

Figure 6: TO-derived topologies using (a): GCMMA, (b): SNOPT and (c): IOPOPT gradient optimizers at *Re*=100, *n*=5 and $v_{fs} = 0.2$.

As for the quantitative comparison between the three TO-derived designs presented in Figure 6, the number of fins is 28 fins, 32 fins, 40 fins for the topologies obtained using the GCMMA, SNOPT and IOPOPT optimizers, respectively, while preserving identical solid fraction (20% solid and 80% fluid) and average fin height (4.1 mm).

3.6 Physical interpretation of the TO-derived geometry

For the purpose of physically interpreting the TO-derived design, the evolution of the densities (porosities) and the Peclet number (*Pe*) distributions with the TO iteration presented in Figure 4c is provided in Figure 7. Considering the nature of density-based TO methodology, a crucial factor, which could determine the solid arrangement, is the relative intensity between the fluidic convective heat transfer and the solid heat conduction within design domain, which can be characterized by this local *Pe* number [43]:

$$Pe = \frac{S(\gamma) \times \boldsymbol{v} \times D_h}{k(\gamma)} \tag{14}$$

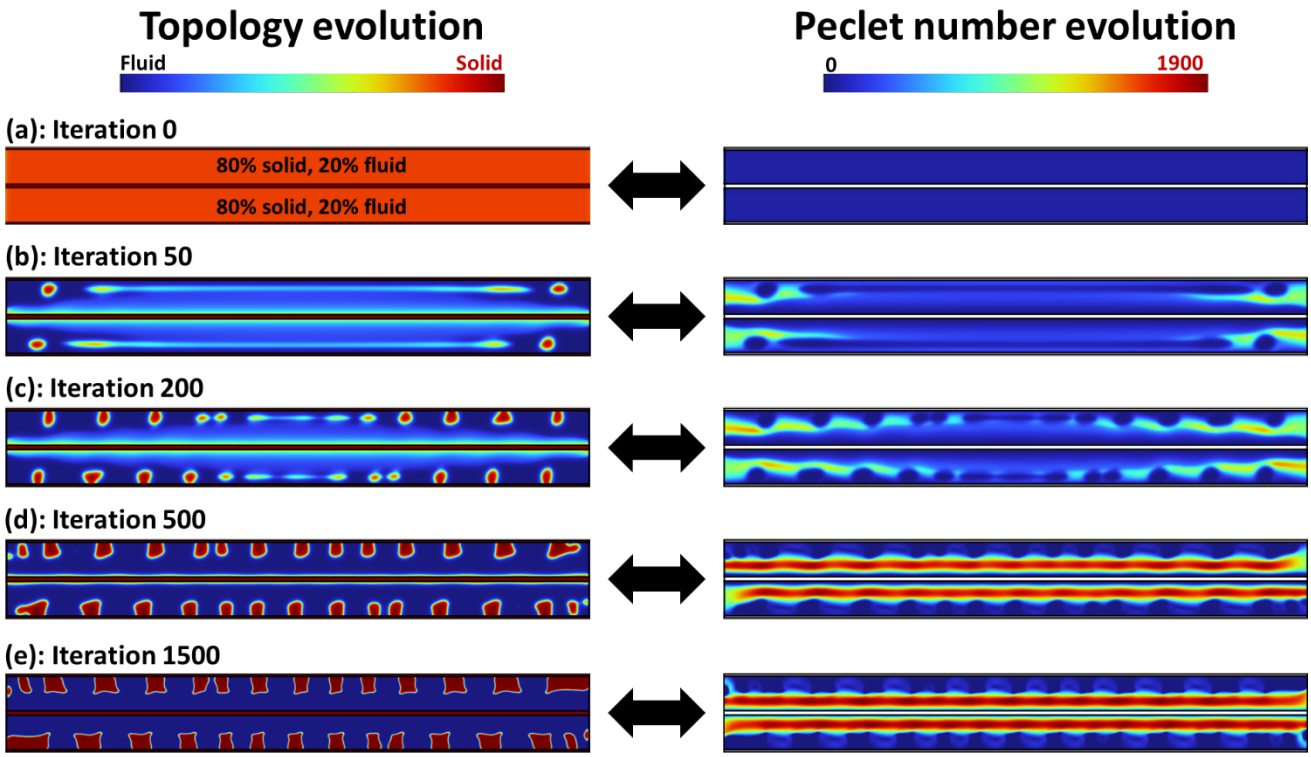

Figure 7: Evolution of the density and the Peclet number distributions in the TO process.

In the flow channels of the HX unit, four high *Pe* number (or velocity) gradient regions can be identified near the walls of the solid plates due to the imposition of non-slip boundary condition. Therefore, the TO optimizer will attempt to position the solid fins within these high Peclet number gradient regions to disturb the flow path, thereby intensifying of the objective function (heat transfer rate). Moreover, since moderate conductive material (SS) is employed in the TO, the optimizer aims to allocate the solids near the insulation and not at the interface wall, leading to a reduction in the conduction resistance of the HX. Furthermore, this solid allocation strives to locally increase the *Pe* number near the walls of the middle plate (where heat is exchanged), consequently resulting in a decrease in the convection resistance of the HX and thereby improving its thermal performance.

3.7 Short summary

In summary, the topologies obtained through TO exhibit sensitivity to variations in input parameters. Furthermore, it is noteworthy that the identical solid allocation in the form of fins persists on both the upper and lower plates of the HX unit, in proximity to the insulation, regardless of the prevailing conditions using moderate conductive material (SS). Additionally, the evolution of the *Pe* number distribution in the TO process demonstrates that this distinct manner of fins allocation aims to increase the local velocity near the HX's interface wall (where heat is exchanged), resulting in a reduction in the convection and conduction thermal resistances and thereby improving the overall heat transfer rate. Lastly, a summary table presenting quantitative information of all obtained topologies is provided as follows.

Table 4: Summary of quantitative information for all acquired topologies

Topology	Solid fraction	Number of fins	Average Fin height (mm)
Figure 2a	20%	42	4.1

Figure 2b	20%	28	4.1
Figure 2c	20%	28	4.1
Figure 3a	20%	34	3.5
Figure 3b	20%	28	4.1
Figure 3c	20%	26	5.5
Figure 4a	20%	28	4.1
Figure 4b	20%	28	4.1
Figure 4c	20%	28	4.1
Figure 4d	20%	26	4.1
Figure 4e	20%	26	4.1
Figure 4f	20%	26	4.1
Figure 5a	5%	28	4.1
Figure 5b	20%	28	4.1
Figure 5c	30%	26	4.1
Figure 6a	20%	28	4.1
Figure 6b	20%	32	4.1
Figure 6c	20%	40	4.1

4. CFD and experimental methods for performance evaluation of TO-derived HX

4.1 3D HX design

The TO-optimized HX unit illustrated in Figure 2b is selected for the present CFD investigation stage and is named TO-optimized HX. Subsequently, a threshold with a 0.5 value (50% solid, 50 % fluid) should be applied on the TO-acquired structure in order to remove the remaining intermediate densities at the solid/fluid interface created by the TO's filtering process as depicted by Figures 8a and 8b [44]. The length of the

optimized HX is increased a few millimeters (9 mm) to avoid the existence of solids at the inlets/outlets boundaries.

Thereafter, the 2D HX unit is extended to 3D as seen in Figure 8c for the purpose of being fabricated and experimentally validated in the forthcoming section. This 3D transformation uniformly extends the 2D HX design in the third direction assuming that the fluid flow effect in the third direction is negligible.

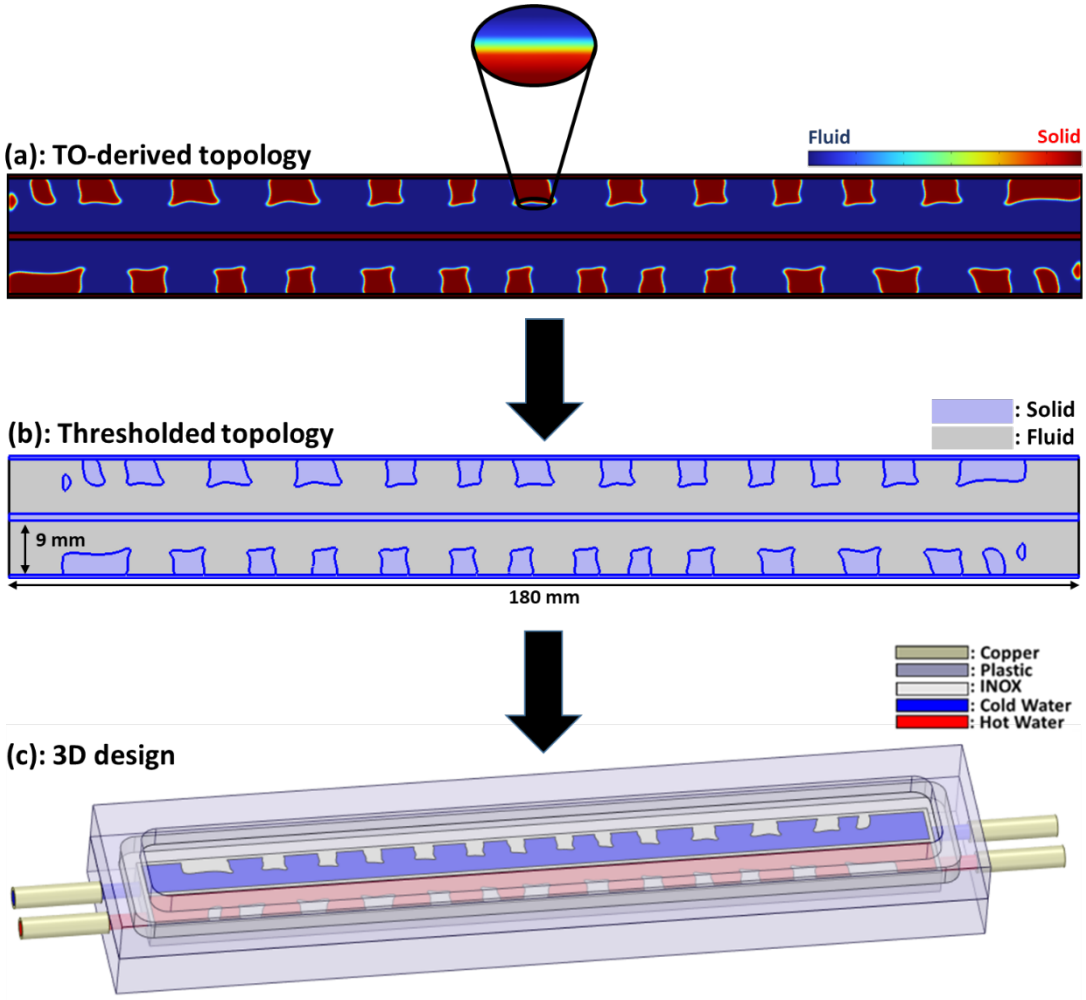

Figure 8: (a): TO-derived structure, (b): Thresholded topology and (c): 3D HX design.

The 3D HX design has a sandwich concept and is decomposed of a plastic cage that covers the HX unit from the bottom and side boundaries to minimize the heat losses to the surrounding. Moreover, the HX unit is covered from the top by a plastic plate with a sapphire window in the middle for IR measurement. The 3D design is illustrated in the figure 9 with the corresponding dimensions and materials.

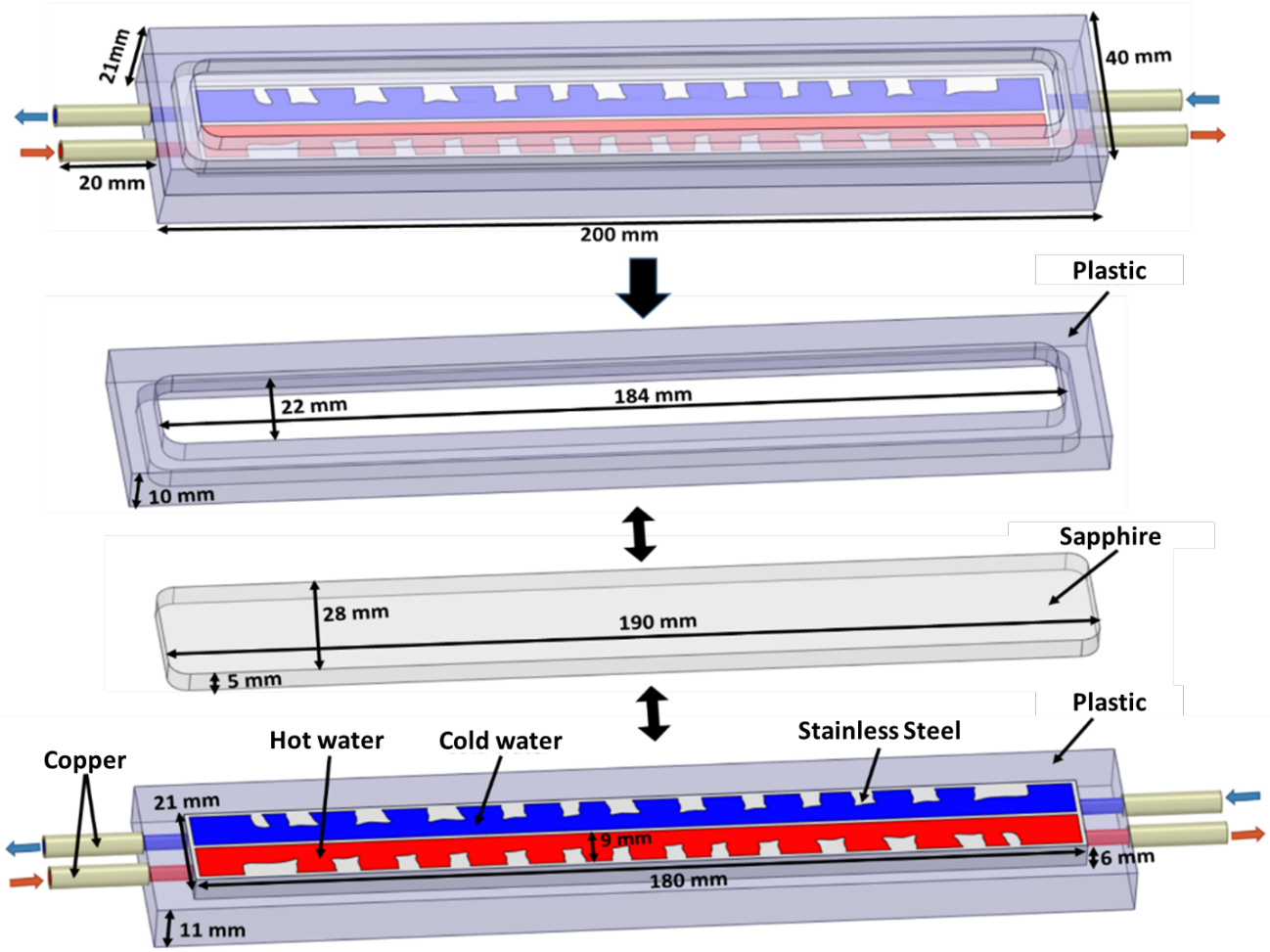

Figure 9: 3D design of TO-HX with the corresponding dimensions and materials.

With the intention of performing a performance comparison with the previously presented TO HX unit, two other HX units that have conventional rectangular fins are introduced as depicted by Fig. 10: one possesses identical fins allocation at the adiabatic boundary and is named Simplified HX unit, and the other has opposite usual fins allocation at the separating wall of hot and cold fluids and is designated as Benchmark HX unit. To make a fair comparison, all HX units (TO-optimized, simplified and

benchmark) have the same solid fraction, external dimensions and materials.

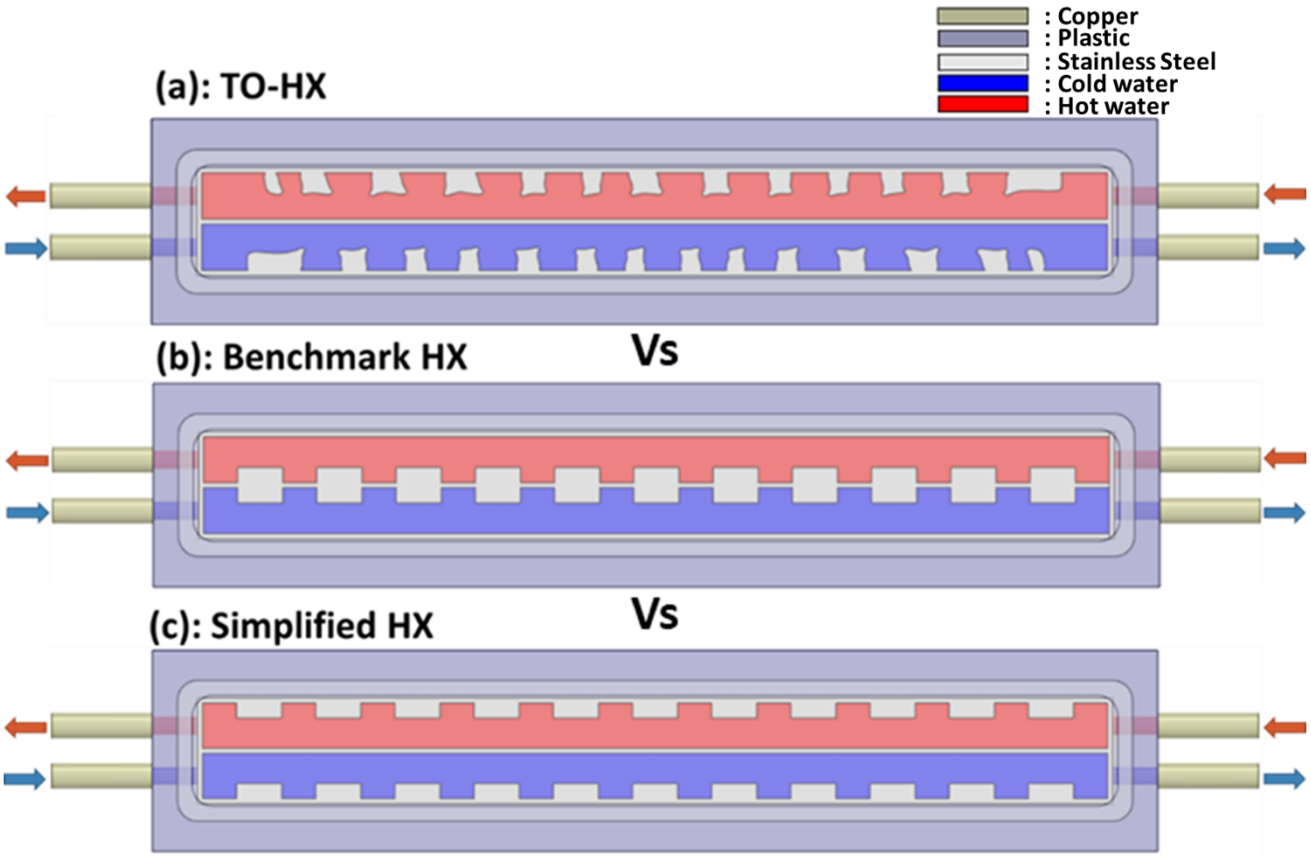

Figure 10: Top view of the **(a):** TO-optimized, **(b):** Benchmark and **(c):** Simplified HX units.

The three investigated HX units (TO-optimized, simplified and benchmark) presented in the previous figure 10 were manufactured using the water jet-cutting machine with a precision of 0.6 mm as depicted by figure 11. As illustrated in the preceding figure 9, the 3D HX design has a sandwich concept composed of a bottom cage made of polycarbonate that surrounds the HX unit fabricated from SS from the side and bottom faces. A sapphire plate was placed at the upper face of the HX unit to authorize optical access for the IR camera, enabling the measurement the temperature distribution. Moreover, a cover plate made of polycarbonate is positioned on the sapphire plate, allowing its fixation using fourteen screws. The detailed dimensions of the bottom cage, HX unit, sapphire plate and cover plates are presented in the figure 9. Lastly, sealing strips were used to avoid the water leakage to the exterior, while strong glue was used at the upper and bottom surfaces of the HX's interface wall to prevent

the mixing between cold and hot fluids.

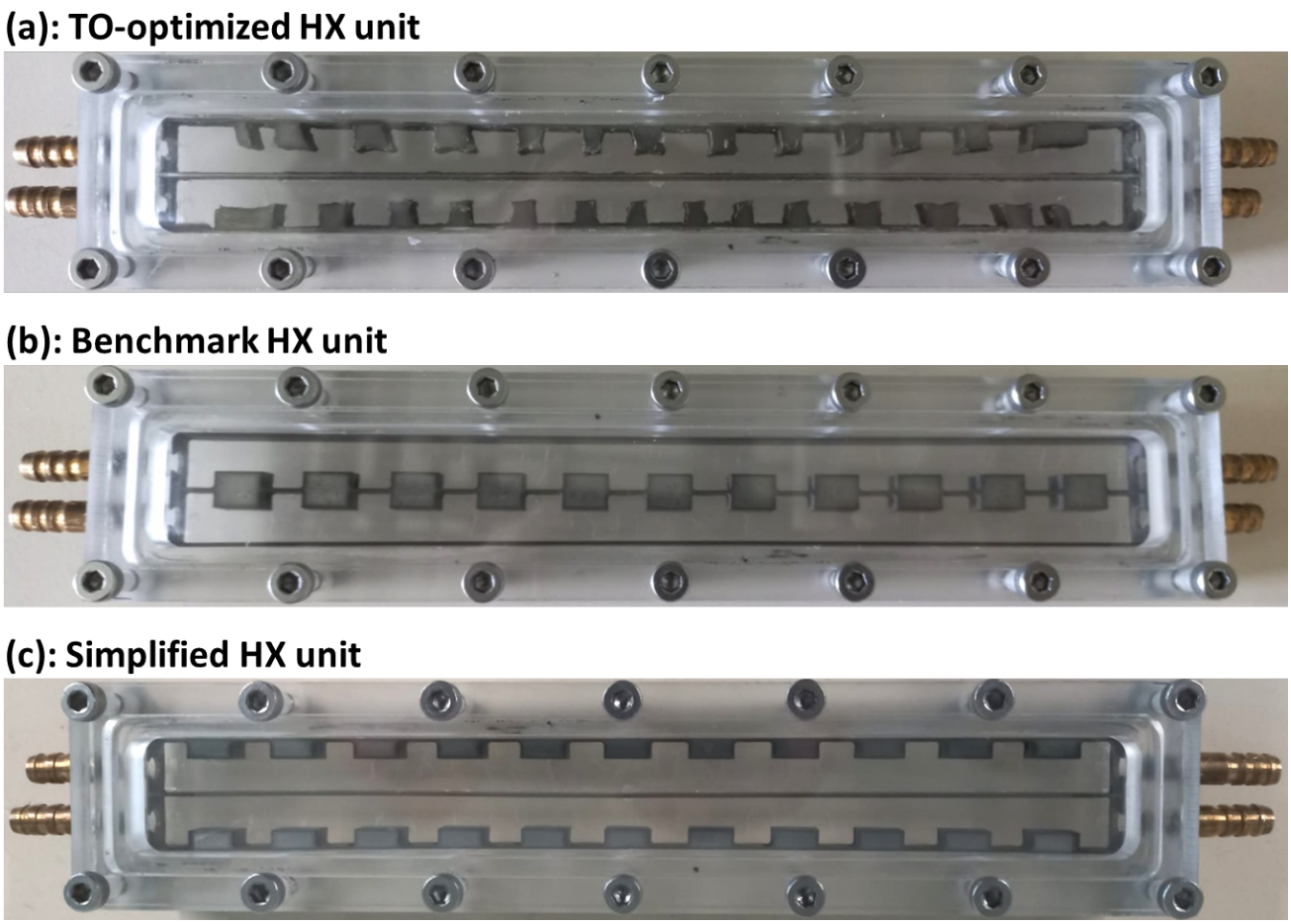

Figure 11: Fabricated **(a):** TO-optimized, **(b):** Benchmark and **(c):** Simplified HX units using the water jet cutting process.

4.2 Computational Fluid Dynamics (CFD) analysis

In this subsection, the detailed methodology of the CFD analysis is presented. First, the geometries of the three HX units (TO-optimized, simplified and benchmark) and the meshes were built using different modules of ANSYS Workbench 19.2. In the present study, the working fluid is set to the water while the solid part of the HX is the SS for maintaining the consistency between the TO and CFD analysis. The bottom cage material is the polycarbonate and the top plates materials are the sapphire and polycarbonate, respectively. The flow connections situated at the inlets and outlets of

the HX unit are comprised of copper material. The thermo-physical properties of the water are considered as temperature dependent, employing the fitting polynomials presented in Table 5. By contrast, the thermo-physical properties of the solids (SS, polycarbonate, polycarbonate and copper) are assumed independent of the temperature as delineated in Table 5. At the inlets of the HX's channels, uniform velocity profile was imposed with inlet temperatures of 288.15 K and 333.15 K for the cold and hot fluids, respectively. The numerical simulations were conducted at ten different flow rates spanning between 0.035 L.min^{-1} and 0.215 L.min^{-1}, which corresponds to $98 \leq \overline{Re_{cold}} \leq 555$ and $180 \leq \overline{Re_{hot}} \leq 1106$, respectively. Moreover, zero static pressure was imposed on the outlets of the HX and no-slip condition was applied on the walls of the flow channels. The bottom and side surfaces of the plastic cage and the side boundaries of the top plastic plate were considered as adiabatic. All other external walls were subjected to a heat transfer coefficient of 7 W.m^{-2}.K^{-1} [20] with an ambient temperature to consider the effect of the natural convection with the surrounding.

The numerical simulations were executed using the FVM (Finite volume method)-solver FLUENT 19.2. The reason of choosing the FLUENT solver for the CFD analysis instead of the FEM-solver of the COMSOL, is the higher numerical stability of the FVM compared to the FEM for simulating the fluid flows [12]. This stability is mainly attributed to the FVM's ability in ensuring the conservation law locally (at each control volume), resulting in a more robust and accurate results. The laminar model was used for low Reynolds number ($\overline{Re_{hot}} \leq 400$), while the turbulent *k-w* SST model [45] was employed for higher $\overline{Re_{hot}}$ (400-1106). The aim of utilizing the turbulent model in the numerical simulations within the theoretical laminar region is mainly to maintain the numerical stability when having local flow vortex, local flow separation and micro-turbulences in the HX's flow channels. The intention of using specifically the *k-w* SST turbulent model, which is a low Re turbulent model, is the superior ability of accurately capturing the flow behavior near the walls compared to high Reynolds number models as (standard k-ε model), especially when having wall separation and flow circulations. Additionally, the *k-w* SST model is widely used in the literature for similar applications

with complex flow patterns and swirls, consistently providing results that align closely with the experimental findings [46]–[49]. The governing equations of the conjugate heat transfer phenomena (Continuity, Momentum and energy equations), along with the turbulence model equations used in the current CFD analysis, are outlined as follows:

$$\begin{gathered}\nabla.\boldsymbol{v} = 0 \text{ (Continuity equation)} \\ \rho_f(\boldsymbol{v}.\nabla)\boldsymbol{v} = -\nabla P + \mu.\nabla^2 v \text{ (Momentum equation)} \\ S_f\boldsymbol{v}.\nabla T - \nabla.(k_s\nabla T) = 0 \text{ (Energy Equation)} \\ \frac{\partial k}{\partial t} + U.\nabla k = P_k - \beta k\omega + \nabla[(\mu + \sigma_k\mu_T)\nabla k] \\ \frac{\partial \omega}{\partial t} + U.\nabla\omega = \alpha S^2 - \beta\omega^2 + \nabla[(\mu + \sigma_\omega\mu_T)\nabla\omega] + 2(1 - F_1)\sigma_{\omega 2}\frac{1}{\omega}\nabla k\nabla\omega\end{gathered} \tag{15}$$

where k is the turbulent kinetic energy (J.kg^{-1}), ω is the specific dissipation rate (s^{-1}), μ_T turbulent viscosity (Pa.s), P_k is the production of turbulent kinetic energy, S is a source term, σ_k and σ_ω are the turbulent Prandtl number for k and ω, respectively, and F_1 is a blending function. As for the velocity-pressure coupling, the standard SIMPLE (semi implicit method for pressure linked equations) was used. The standard method was utilized for the space discretization of the pressure field, while the first order upwind scheme was used for velocity and temperature field discretization. For the turbulent equations *k* (kinetic energy) and *w* (specific rate of dissipation) discretization, the second order upwind scheme was chosen to decrease the fluctuation of the turbulent equation's residuals leading to an enhanced convergence rate. The solution is judged to be converged when the residuals of all governing equations are less than 1e-5 (the residual of the energy equation is less than 1e-8) and the iterative variation of the inlet static pressure and the outlet temperature of the cold fluid is below 0.5 %. A mesh dependency study was conducted following the same methodology of Celik et al. [50] to ensure the reliability of the numerical results. Moreover, the stopping criteria of the mesh sensitivity analysis are outlined as follows:

$$Er(\Delta P) = \left|\frac{\Delta P^k - \Delta P^{k+1}}{\Delta P^k}\right| < 1\% \ \& \ Er(T_{out}) = \left|\frac{T^k_{out,cold} - T^{k+1}_{out,cold}}{T^k_{out,cold}}\right| < 1\% \tag{16}$$

where *k* is the index of the mesh dependency test, ΔP is the pressure drop in the cold

channel of the HX unit (Pa), $T_{out,cold}$ is the cold flow outlet temperature (°C) and Er is the relative error. As an example, for $\overline{Re_{hot}}$= 1106 ($\overline{Re_{cold}} = 555$), the details about the mesh dependency study are given in Table 6 for the TO-optimized HX unit. Accordingly, the results are considered to be mesh independent when the number of elements hit 13.38 million, 13.07 million and 12.97 million for the optimized, benchmark and simplified HX units, respectively. Lastly, it is noteworthy to mention that the constructed mesh presented in Figure S2 is composed of tetrahedron elements and presents a good quality with an average skewness of 0.22. The mesh in the fluid domains is much finer compared to the one the solid one and eight inflation layers have been used in the fluid domains to accurately capture the velocity gradient near the walls as depicted by Figure S3.

Table 5: Physical properties of the fluid and solids used for the numerical simulations (283.15 K <T< 343.15 K) [40]–[43]

Water	*Density [kg.m^{-3}]*	$\rho = -3.3 \times 10^{-7}T^4 + 4.3 \times 10^{-4}T^3 - 0.217T^2 + 47.95T + 2962.83$
	Specific heat [J kg^{-1} K^{-1}]	$C_P = 4.81 \times 10^{-6}T^4 - 6.1 \times 10^{-3}T^3 + 2.98T^2 - 643.2T + 56148.51$
	Viscosity [Pa.s]	$\mu = 2.96 \times 10^{-11}T^4 - 4 \times 10^{-8}T^3 + 2 \times 10^{-5}T^2 - 4.6 \times 10^{-3}T + 0.4$
	Thermal conductivity [W m^{-1} K^{-1}]	$k = -6.4 \times 10^{-11}T^4 + 1.34 \times 10^{-7}T^3 - 9.91 \times 10^{-5}T^2 + 3.2 \times 10^{-2}T - 3$
Copper	*Density [kg.m^{-3}]*	$\rho = 8850$
	Specific heat [J kg^{-1} K^{-1}]	$C_P = 392$
	Thermal conductivity [W m^{-1} K^{-1}]	k =398
Polycarbonate	*Density [kg.m^{-3}]*	$\rho = 1200$
	Specific heat [J kg^{-1} K^{-1}]	$C_P = 1100$
	Thermal conductivity [W m^{-1} K^{-1}]	$k =$ 0.2
Sapphire	*Density [kg.m^{-3}]*	$\rho = 3980$
	Specific heat [J kg^{-1} K^{-1}]	$C_P = 763$
	Thermal conductivity [W m^{-1} K^{-1}]	$k = 37$
SS	*Density [kg.m^{-3}]*	$\rho = 7800$
	Specific heat [J kg^{-1} K^{-1}]	$C_P = 468$
	Thermal conductivity [W m^{-1} K^{-1}]	$k = 15$

Table 6: Mesh dependency test for the TO-optimized HX unit at $\overline{Re_{hot}}$= 1106

Elements number	ΔP (Pa)	Error (ΔP) (%)	$T_{out,cold}$ (°C)	Error ($T_{out,cold}$) (%)
2,773,467	291.883	--	22.098	--
6,093,309	270.538	7.31 %	21.02	4.87 %

13,387,038	261,012	3.52 %	20.54	2.28 %
29,495,860	258.47	0.97%	20.401	0.67%

4.3 Experimental approach

4.3.1 Experimental set-up

Figure 12 illustrates the experimental setup built in the LTeN laboratory for the aim of experimentally evaluating the thermo-hydraulic performance of TO-optimized, benchmark and simplified HX units. The setup permits the circulation of the cold and hot pure water with controlled inlet temperatures and flow rates thanks to two LAUDA RP855. Two manual valves were installed at the discharge section of each LAUDA RP855 for more control precision of the flow rate. Furthermore, a Kobold DPM-1103 flow meter (± 2.5% precision) was located at

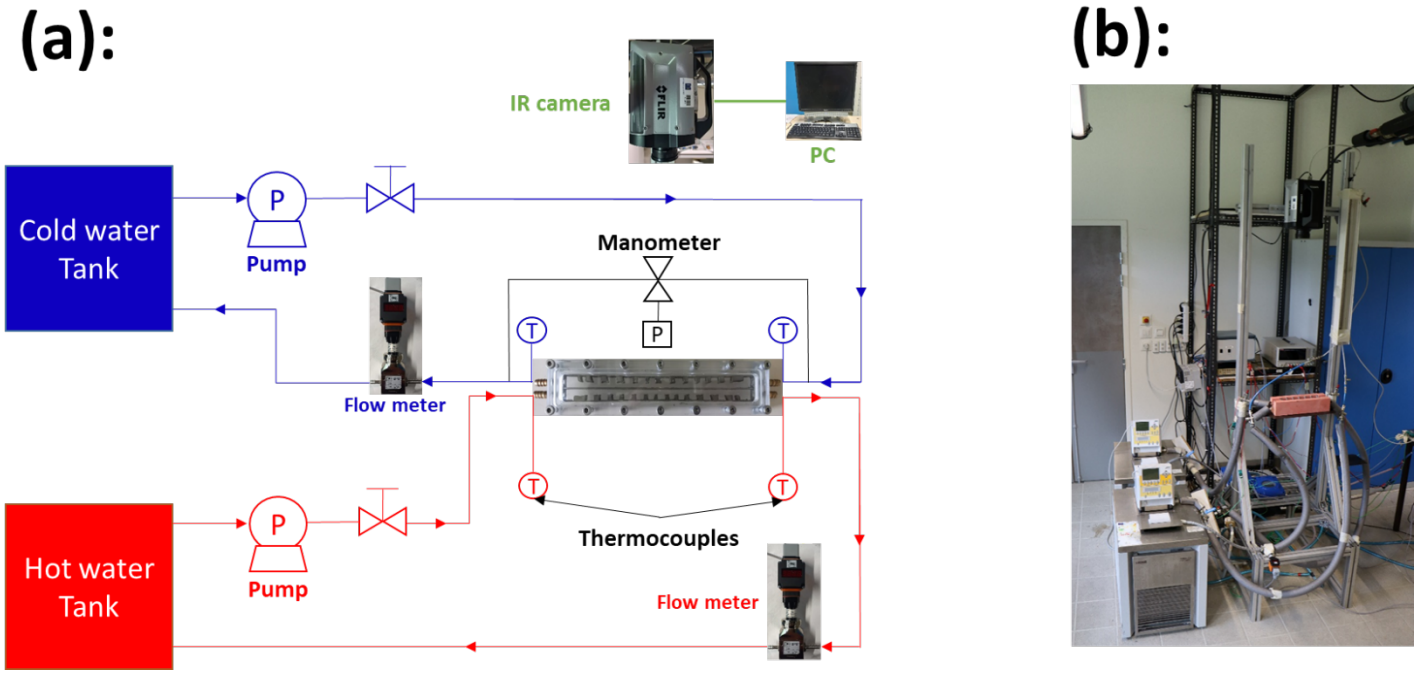

Figure 12: (a): Schematic view and **(b):** Photo view of the experimental setup built in the LTeN laboratory.

the suction section of each LAUDA in each circuit (cold and hot) to measure the flow rate. The inlet and outlet temperatures of the hot and cold fluids were measured using four thermocouples of type K ($\pm$ 0.2K precision) and a central acquisition system with an acquisition frequency of 0.1 seconds.

The hydraulic performance of the HX units was experimentally evaluated by measuring the static pressure at the inlets and outlets of the HX's cold and hot channels using a vertical manometer. Lastly, an IR camera has been used to measure and compare the local temperature field at the targeted surface.

4.3.2 Infrared thermography and measurement schemes

In the present work, the Infrared (IR) thermography is employed to measure the fluid temperature distribution at the local scale, which is then compared with the one evaluated by the CFD analysis for validation purposes. The fundamental principal of the IR thermography lies in the detection of radiation emitted by an object through infrared lens, which is subsequently converted to an electrical signal. Following amplification and data processing, the signal ultimately undergoes a transformation to display the temperature distribution values. According to the literature [51], most of the used IR camera are sensitive in the middle and long wavelength ranges. In the present study, the employed IR camera (FLIR, X-series) can detect radiation with a wavelength spanning from 1.5 μm to 5 μm. Within this range, the sapphire plate with a 5 mm has a transmission over 60 % [52], while the

emissivity of the water ranges between 0.92 and 0.96 [53]. Hence, the IR camera is capable of detecting the thermal radiation emitted by the water via the sapphire window.

At each operating flow rate, the temperature and pressure measurements were carried out once the steady-state has been achieved, i.e., the outlet temperature of the cold fluid is stable. Upon reaching the thermal stability (steady-state), a real time image recording was performed using the commercial software ResearchIR with a frame frequency of 60 Hz. After obtaining 1000 successive temperature images (matrices), an element-wise average was performed to acquire the final measured temperature field with a resolution of 82×512 pixels. As depicted in figure S1 (section S1 of the supplementary material document), the selection of 1000 images was sufficient to obtain a stable temperature contour. Moreover, it is noteworthy to mention that the IR measurement targets the inner surface of the sapphire plate (targeted surface) that is in direct contact with the water inside the HX. This is because the IR radiation can be transmitted through the semi-transparent sapphire, but not through the water. Lastly, the temperature fields of the solid phase measured by the IR camera at the targeted surface must be hidden using the solid phase coordinates within the HX's domain.

4.3.3 Uncertainty analysis

An uncertainty analysis was performed, employing the methodology of Moffat [54] to quantify the uncertainties of the experimental approach. Moffat [54] estimated the error between the mean value (true value) for different repeated trials and the measured value to be the twice of the standard deviation ($\pm 2\sigma$) for single sample experiments.

Therefore, the experiments have been repeated three times first, showing an acceptable uncertainty of the experimentally measured heat transfer rate and friction coefficient with an error up to $\pm 4.15\ \%$ and $\pm 4.38\ \%$ for the TO-optimized HX unit, up to $\pm 4.65\ \%$ and $\pm 4.95\ \%$ for the simplified HX unit, and up to $\pm 4.77\ \%$ and $\pm 5.07\ \%$ for the benchmark HX unit, respectively. The reason of repeating the experiments only three times due to the acceptable volatility error observed in the recurring experimental measurements of the heat transfer rate and friction coefficient. Eventually, it is noteworthy to mention that the uncertainty associated with the thermocouples is about $\pm 1.3\ \%$, while the uncertainty of the flow meter is approximately $\pm 2.5\ \%$.

5. Results and discussions

5.1 Thermo-hydraulic performance evaluation and validation

First, the Reynolds number of the cold and hot fluids is calculated based on the area-averaged flow properties and velocities inside the HX's flow channels using the following equation:

$$\overline{Re} = \frac{\overline{\rho_f}.\bar{v}.Dh}{\bar{\mu}} \tag{17}$$

where $\overline{\rho_f}$ is the fluid average density (kg.m^{-3}), $\bar{\mu}$ is the fluid average dynamic viscosity (Pa.s), $\bar{v}$ is the volume-weighted average velocity inside the cold or hot flow channels (m.s^{-1}) and Dh is the hydraulic diameter calculated according the cross-sectional dimensions of the HX's flow channel which is equal to 0.0072 m.

The heat transfer rate on the cold fluid side is utilized as a criterion to evaluate the HX's thermal performance and is calculated using the following equation:

$$Q = \dot{m}\overline{C_p}(T_{out} - T_{in}) \tag{18}$$

where Q is the heat transfer rate (W), $\dot{m}$ is the mass flow-rate of the cold fluid

(kg.s^{-1}), T_{out} and T_{in} are the mass-flow average temperatures at the outlet and inlet of the cold fluid (K), respectively, and $\overline{C_p}$ is the average specific heat of the cold flow channel (J.kg^{-1}.K^{-1}). The highest observed heat loss to the ambient, calculated by the difference between the heat transfer rates on the hot and cold sides, is approximately 4% (1.32W) at the lowest flow rate (0.035 L.min^{-1}). This small percentage indicates that the heat losses have a negligible effect on the evaluation of the HX's thermal performance. As seen by Fig. 13, a good agreement between the heat transfer rate evaluated experimentally (through four thermocouples and flowmeters) and numerically (CFD analysis) has been observed, with a maximum deviation up to 3.5%, 4.81% and 5.61% for the TO-optimized, simplified and benchmark HX unit, respectively. Results demonstrate a higher exchanged heat in the TO-optimized and simplified HX units compared to the benchmark case with an enhancement up to 18.09% and 10.23 %, respectively. This validates and confirms the thermal efficacy and superiority of the TO-optimized and simplified design that are mainly featured by the solid allocations proximate to the insulation over the benchmark configuration typified by the solid positioning on the HX's interface wall.

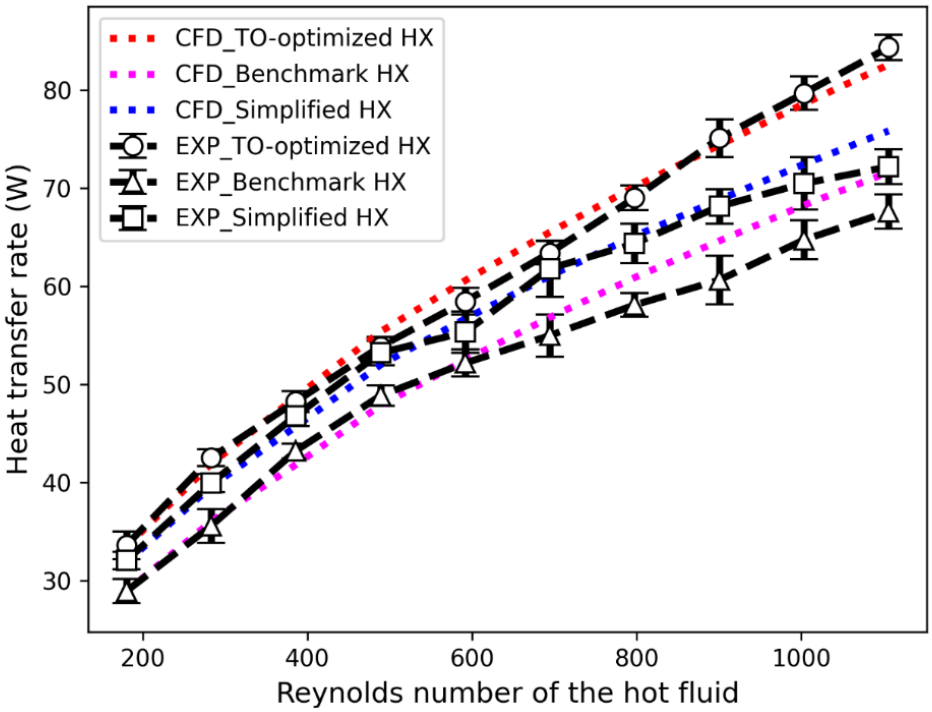

Figure 13: Variation of the heat transfer rate of the three HX units evaluated numerically and experimentally with respect to *Re*.

Moreover, the pressure drop is experimentally measured using a vertical manometer to validate and compare it with that evaluated through the CFD analysis. Thereafter, the friction coefficient can be directly computed from the measured pressure drop as follows:

$$f = \frac{2\Delta P D_h}{\overline{\rho_f} l \bar{v}^2} \tag{19}$$

where ΔP is the pressure drop (Pa) and l is the length of the HX (m). As illustrated by Fig 14, a noteworthy concurrence between the friction coefficients evaluated experimentally and numerically (CFD) for all designs is evident with a maximum deviation up to 5.5%, 5.78% and 6.17% for the TO-optimized, simplified and benchmark HX units, respectively. This deviation is considered as acceptable (<1%) regarding the experimental uncertainty for the friction coefficient. Moreover, the

error bars of the three-plotted curves in Figure 14 overlaps between each other at different flow rate conditions. This elucidates the small difference in the measured friction coefficient of the three HX units, confirming the slight increase in the hydraulic losses predicted numerically of the TO-optimized HX units compared to the simplified and benchmark designs.

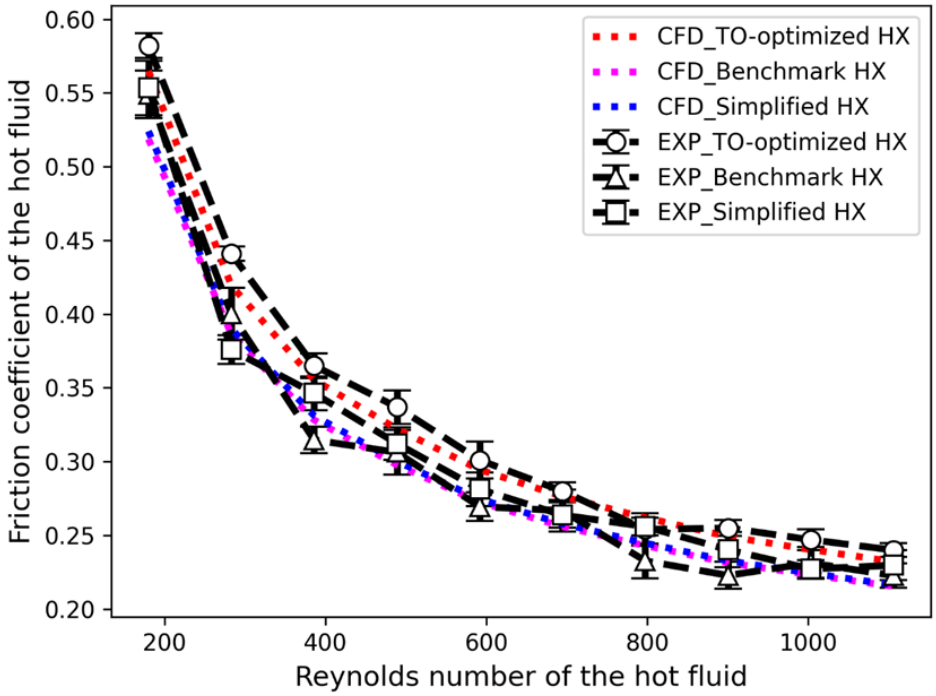

Figure 14: Variation of the friction coefficient of the three HX units evaluated numerically and experimentally with respect to the *Re*.

To consider the thermo-hydraulic performance simultaneously, the heat transfer rates for the three HX configurations are plotted as a function of the pumping power (Q_{pump}) calculated thought the following equation:

$$Q_{pump} = (\dot{v}\Delta P)_{cold} + (\dot{v}\Delta P)_{hot} \quad (20)$$

where $\dot{v}$ is the volumetric flow rate ($m^3.s^{-1}$). As seen by Figure 15, a notable agreement between the numerical and experimental plots is conspicuous, substantiating the thermo-hydraulic performance advantage of the TO-optimized

HX unit over the simplified and benchmark cases with a heat transfer intensification up to 8.7 % and 15.08 % under the same pumping power, respectively.

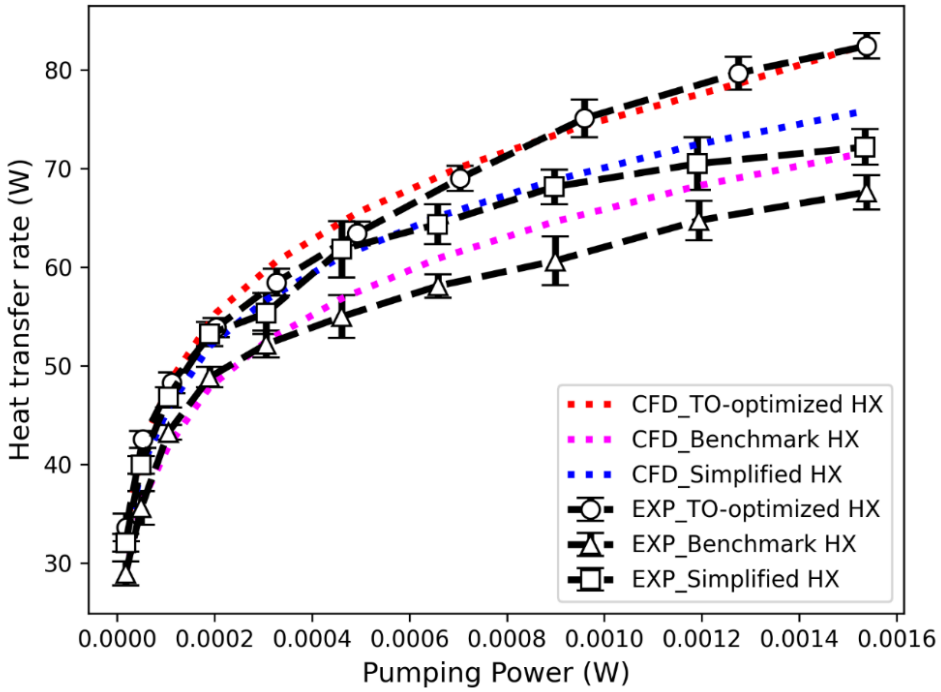

Figure 15: Evolution of the heat transfer rate computed experimentally and numerically with respect to the Pumping power.

By summarizing this subsection, the thermo-hydraulic performance of the TO-derived design is experimentally evaluated and compared with the numerical results acquired through CFD analysis. The comparison illustrates a good agreement between numerical and experimental results with acceptable deviations. This serves to confirm and substantiate that the optimal allocation of the low/moderate conductive solids for obtaining maximized thermo-hydraulic performance is in proximity to the insulation (as in the optimized and simplified designs) and not at the HX's interface wall (as in the benchmark design).

5.2 Comparison between CFD and IR camera results (Fluid local temperature distribution comparison and validation)

- Fluid Temperature contours

Figures 16a, 16b & 16c expose the fluid temperature contours measured by the IR thermography and Figures 16d, 16e & 16f illustrate those acquired through the CFD analysis for the TO-optimized, benchmark and simplified HX units, respectively, under the same volumetric flow rate of 0.135 L.min^{-1} ($\overline{Re_{cold}}$ = 354, $\overline{Re_{hot}}$ = 695). For the three HX units, the isotherms acquired through IR camera and CFD exhibit a well correspondence, on the global range. As seen by Figure 16, the main differences in the IR and CFD isotherms can be observed at the solid/fluid interfaces. Moreover, the isotherms computed numerically tend to move forward in the flow direction compared to the one measured through the IR camera. As for the TO-optimized HX unit, the minimum and maximum temperatures measured at the targeted surface are 290.68 K (CFD), 291.83 K (IR) and 331.23 K (CFD), 330.14 K (IR), respectively. Moreover, the minimum and maximum temperatures measured at the targeted surface of the simplified HX unit are 292.9 (CFD), 293.25 K (IR) and 329.09 K (CFD), 328.2 K (IR camera), respectively. As for the benchmark case, the minimum and maximum temperatures observed at the targeted surface are 293.9 (CFD), 294.5 K (IR) and 328.09 K (CFD), 327.047 K (IR). This small difference (about 1 K) between the border temperatures of the cold and hot fluids for the three HX units serve as additional evidence to authenticate the well conformity between the local temperature distributions evaluated numerically (CFD) and experimentally

(IR camera).

By comparing the temperature contours of the three different HX units, a higher temperature gradient (The difference between the highest temperature of the hot fluid and the lowest temperature of the cold fluid at the targeted surface) between the cold and hot fluids has been observed in the TO-optimized (38.31 K) and simplified (34.95 K) HX units compared to the benchmark HX unit (32.547 K). A heightened temperature gradient signifies an elevated exchanged heat between the two fluids, confirming the superior thermal performance of the TO-optimized and simplified designs over the benchmark case.

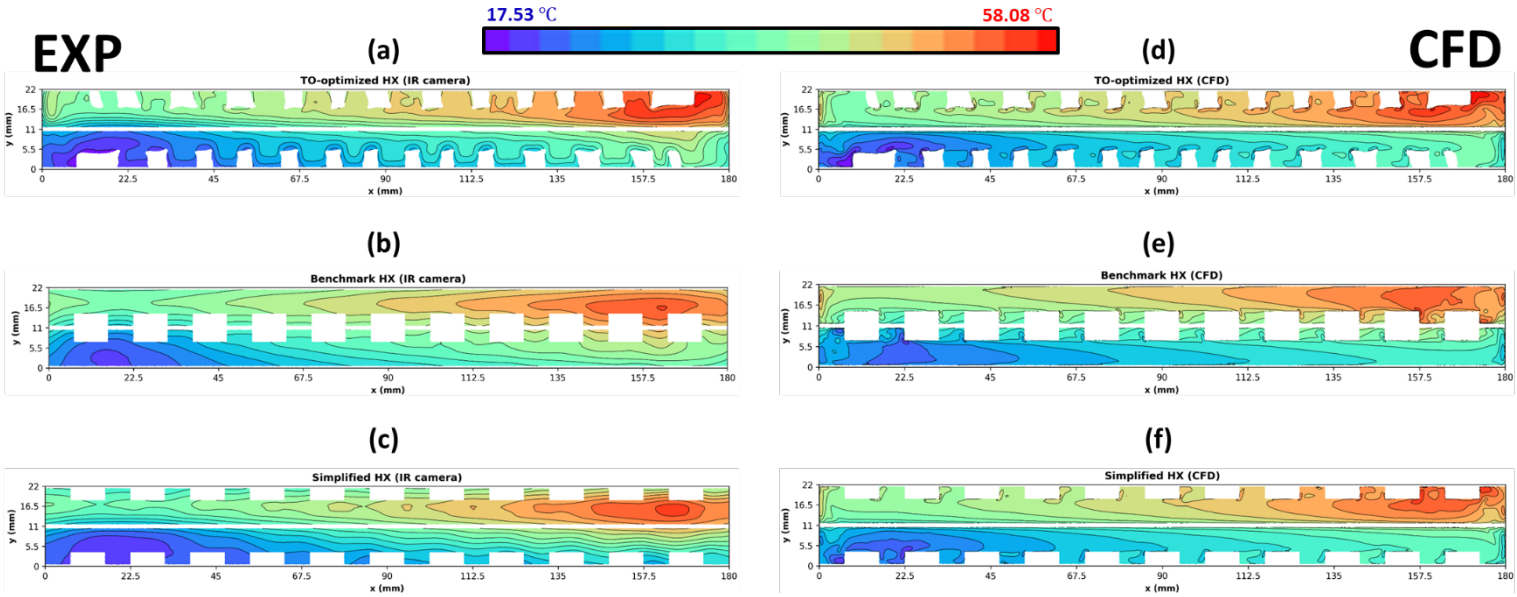

Figure 16: Comparison between the temperature contours acquired through IR measurements and CFD analysis for the three HX units at $\overline{Re_{cold}}$ = 354, $\overline{Re_{hot}}$ = 695.

- Local Temperature along sampling lines

For further analysis and comparisons between IR thermography measurement and CFD analysis, the local temperature profiles of the TO-optimized HX unit are compared and plotted as seen in Figure 17 at two sampling lines: one for the cold fluid at the position of y=7 mm and the other for the hot fluid at the position of y = 15.8 mm and x spans from 0 mm to 180 mm for both sampling lines.

Evidently, the IR and CFD local temperature profiles are generally corresponded, for both sampling lines. Nonetheless, two peak deviations between the IR and CFD curves can be observed once for the cold fluid sampling line at x= 169 mm (about 13.8%) and the hot sampling line at x=0.5mm (about 21.75%). The reason behind this relatively high discrepancy may arise from the limitation of the fabrication precision in manufacturing small channels with complicated geometries. Moreover,

the difference between the velocity profiles between the CFD analysis and

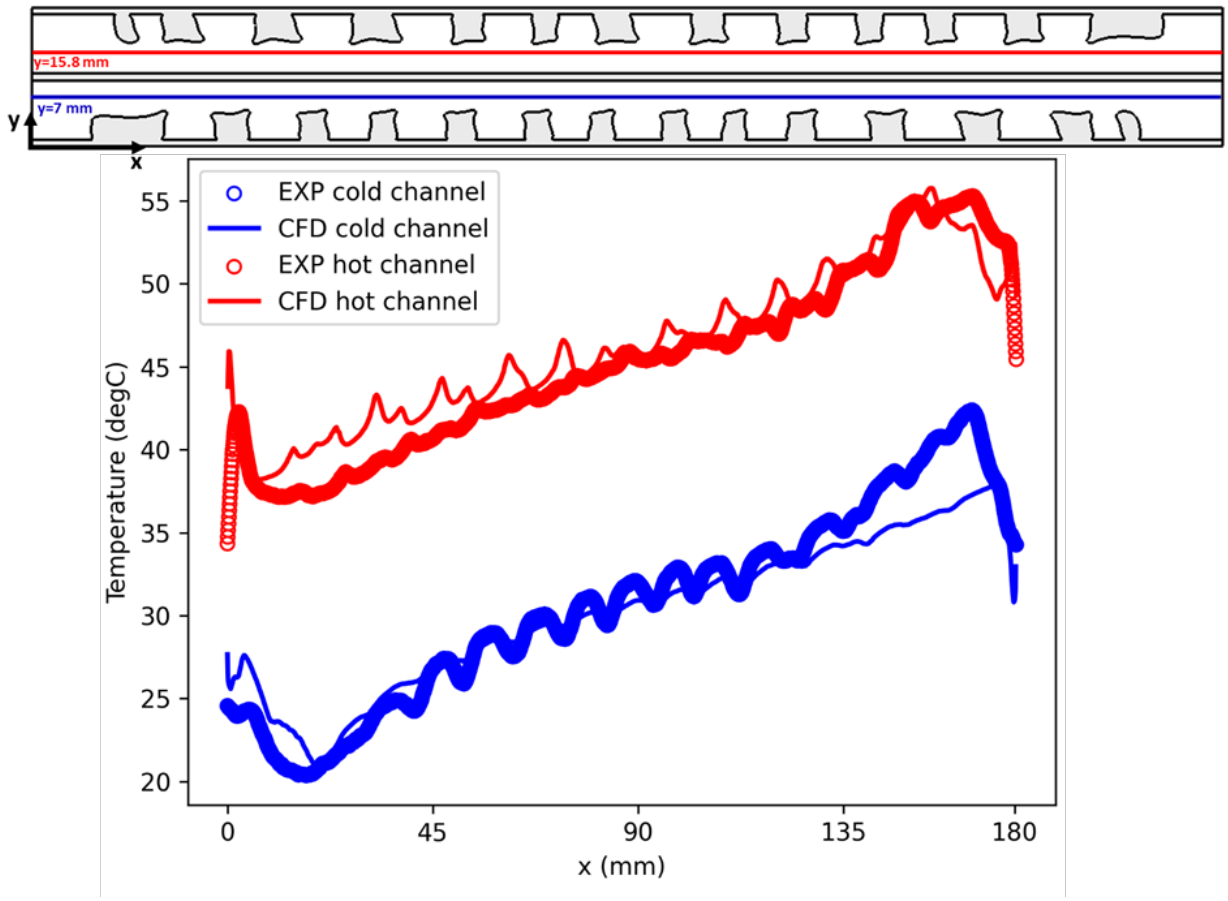

Figure 17: Comparison of the local temperature profiles at different sampling lines of the TO-optimized HX unit at $\overline{Re_{cold}} = 354$, $\overline{Re_{hot}} = 695$.

experimental at the inlets of the HX could be also another possible reason. Nevertheless, by visualizing the figure, it is apparent that the IR and CFD curves generally match at the majority of x positions. The mean errors for both cold and hot fluids sampling lines yield percentages of approximately 4.45% and 3.3 %, respectively, which underscores the consistency between CFD and experimental curves.

Following the same strategy, the local temperature profiles evaluated

experimentally (IR camera) and numerically (CFD) for the simplified HX unit are compared as illustrated in Fig. 18 along two sampling lines: one for the cold fluid at

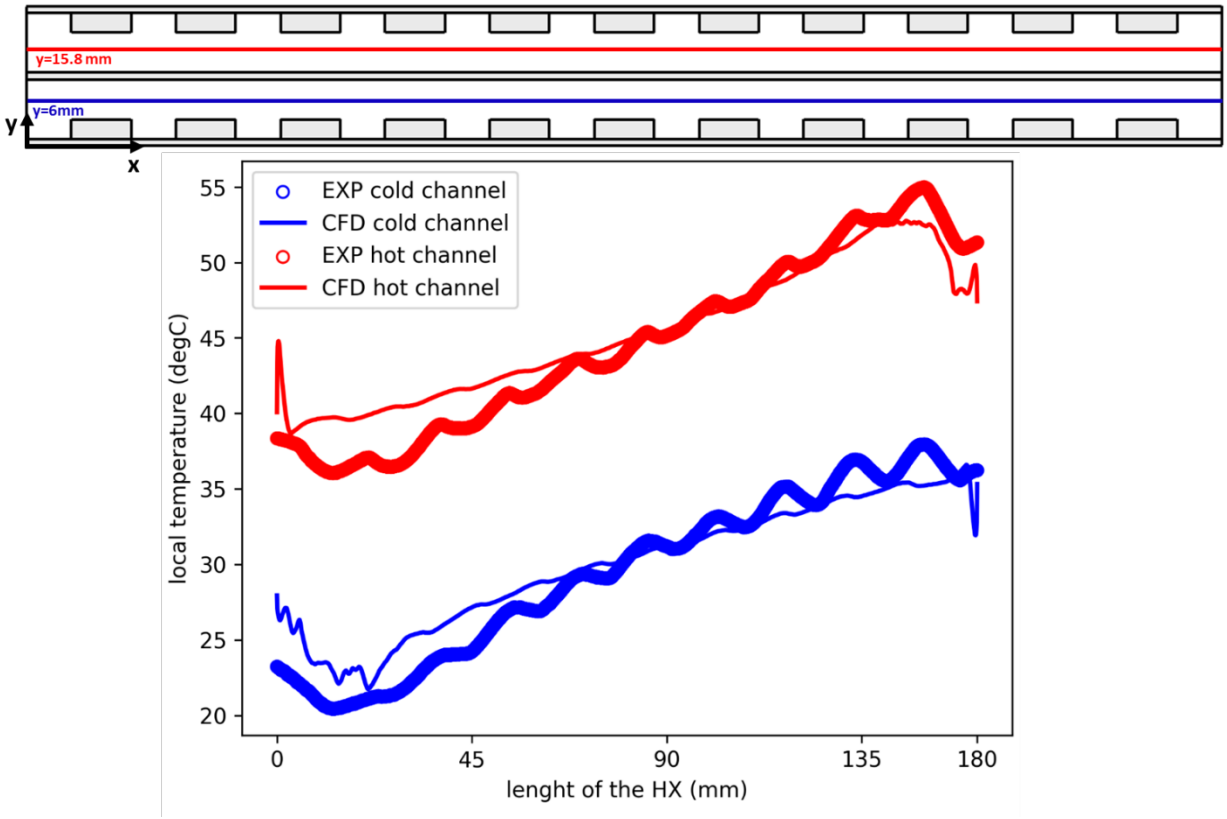

Figure 18: Comparison of the local temperature profiles at different sampling lines of the simplified HX unit at $\overline{Re_{cold}} = 354$, $\overline{Re_{hot}} = 695$.

the position of y=6 mm and the other for the hot fluid at the position of y = 15.8 mm and x spans from 0 mm to 180 mm for both sampling lines. A good consistency is evident between the temperature curves evaluated numerically and experimentally along the HX length. The maximum deviations observed in the temperature contours along the cold and hot sampling line are 16.8 % (x=0 mm) and 14.3 % (x=175 mm), respectively. Additionally, the mean error between the numerical and experimental temperature profiles along the cold and hot sampling lines are 5.1% and 3.5 %, respectively, which authenticates the good concordance between the numerical and experimental temperature profiles for the simplified HX

unit.

Lastly, the temperature profiles of the benchmark HX unit evaluated numerically and experimentally are also compared along two sampling lines: one for the cold fluid at the position of y=3 mm and the other for the hot fluid at the position of y = 15.8 mm and x spans from 0 mm to 180 mm for both sampling lines. The numerical and experimental temperature profiles exhibit a good match along both sampling lines as depicted by Fig. 19. The maximum deviation between numerical and experimental curves at the cold sampling line is 11.6% (x=172 mm) and 12.29% (x=3 mm) along the hot sampling line. Unlike the previous presented plots for the TO-optimized and simplified HX units, the CFD and IR temperature profiles of the cold fluid in the benchmark design do not match well at the global trend. The reason behind this discrepancy may be attributed to experimental or numerical uncertainties. Nevertheless, the mean absolute errors calculated at the cold and hot sampling lines are 7.5% and 3.1 %, respectively. This confirms the consistency

between the numerical and experimental temperature profiles for the benchmark HX unit.

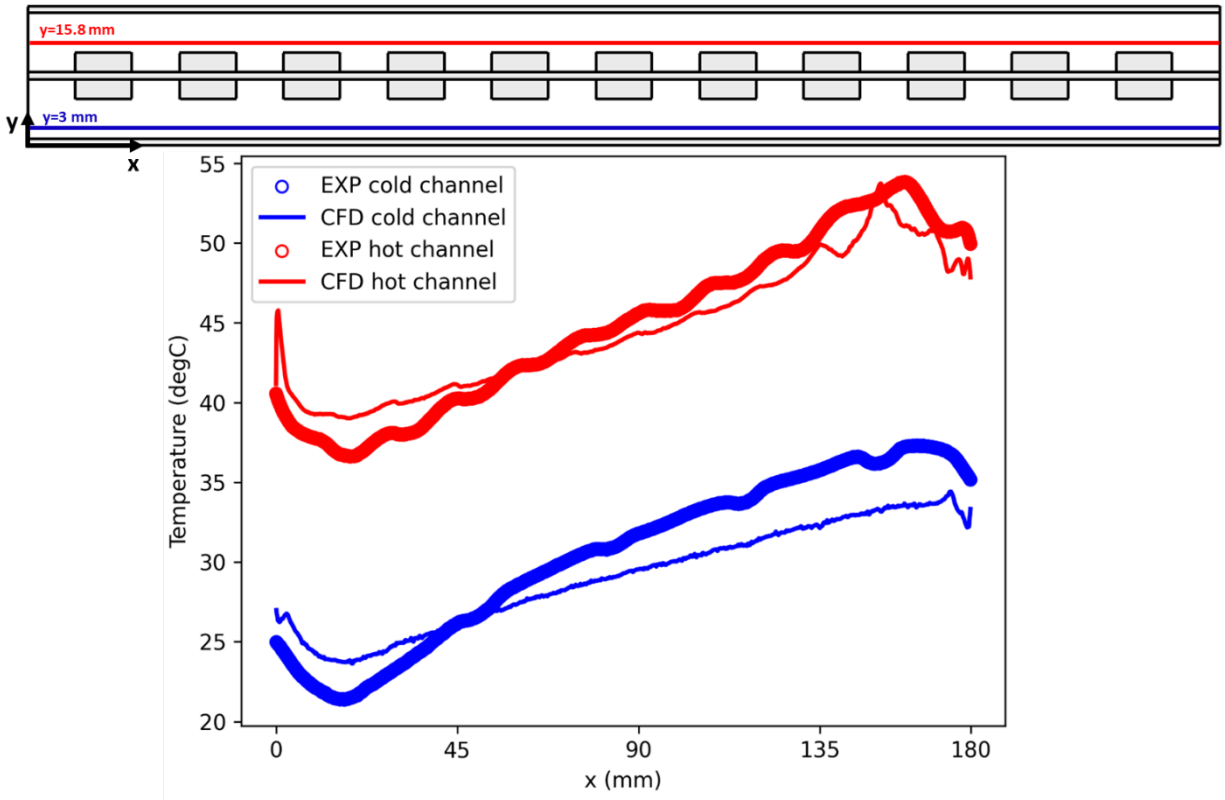

Figure 19: Comparison of the local temperature profiles at different sampling lines of the benchmark HX unit at $\overline{Re_{cold}} = 354$, $\overline{Re_{hot}} = 695$.

As a summary, the local temperature profiles for the three HX units measured experimentally using the IR camera and evaluated numerically through the CFD analysis are compared, showing a good agreement between each other. This serves as an additional evidence to prove the high fidelity of the CFD analysis in evaluating the heat transfer characteristics of the three investigated HX units at the local level.

5.3 Physical interpretation

In this subsection, the heat transfer intensification exhibited in the TO-optimized and simplified HX units is physically interpreted. First, the velocity contours evaluated through the CFD analysis are plotted on the three HX units

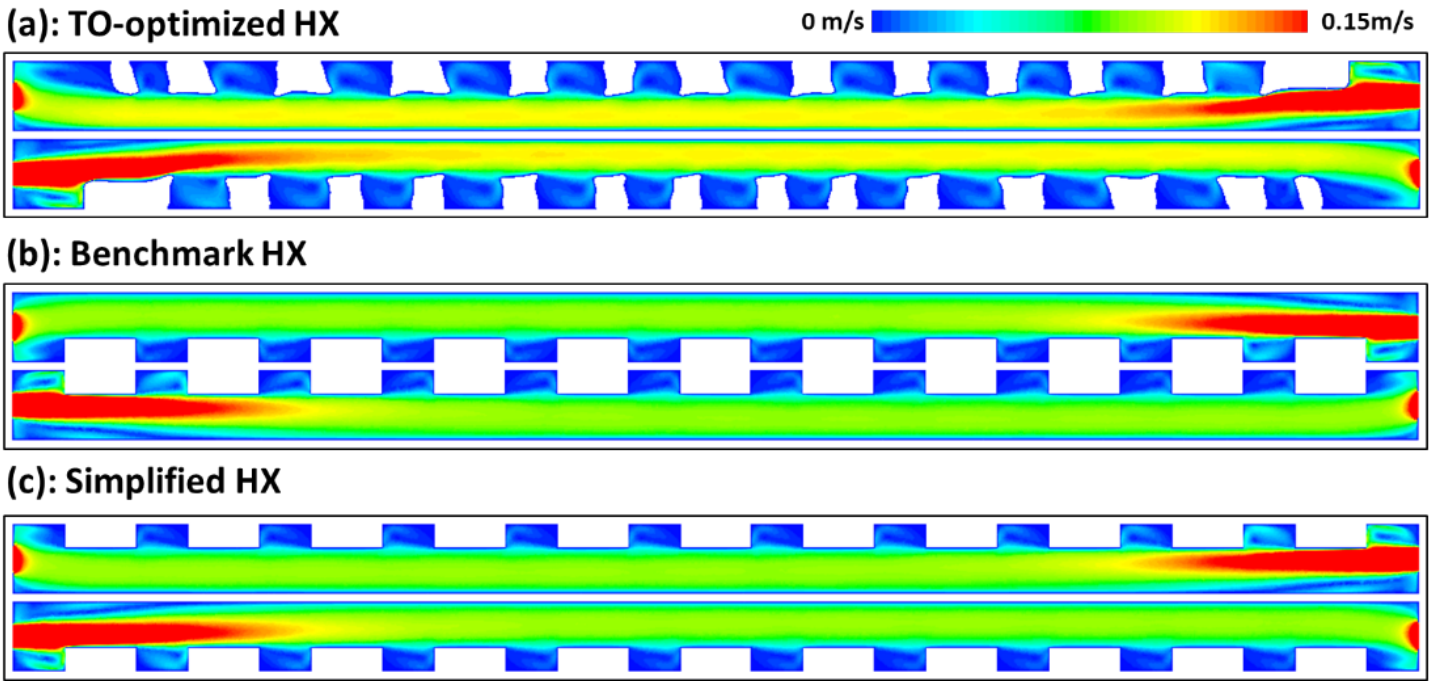

Figure 20: Velocity contours of the **(a):** TO-optimized, **(b):** Simplified and **(c):** Benchmark HX units at $\overline{Re_{hot}}$= 695.

(optimized, simplified and benchmark) at $\overline{Re_{hot}}$= 695 as seen in Figure 20.

Apparently, the optimized and simplified designs attempt to increase the velocity locally near the interface where heat is exchanged between two fluids, leading to a decrease in the convective thermal resistance and thus an augmentation in the overall thermal performance. By contrast, the benchmark design seeks to disturb the fluid near the interface wall but actually results in numerous dead zones between the solids, leading to an increase in the convective thermal resistance and thus a decrease in the overall thermal performance. Furthermore, allocating the

solids at the interface wall as in the benchmark design will directly increase the conduction thermal resistance and thus will decrease the thermal performance notably when using low or moderate conductive material as in the present case (SS). In order to confirm the previous mentioned interpretations, the overall thermal resistance (R_{th}) is calculated for the three HX units using the following equation:

$$R_{th} = \frac{\Delta T_m}{Q} \tag{21}$$

where ΔT_m is the logarithmic mean temperature difference (K) calculated as follows:

$$\Delta T_m = \frac{\left(T_{in,hot} - T_{out,cold}\right) - \left(T_{out,hot} - T_{in,cold}\right)}{ln\frac{\left(T_{in,hot} - T_{out,cold}\right)}{\left(T_{out,hot} - T_{in,cold}\right)}} \tag{22}$$

where $T_{in,hot}$ and $T_{out,hot}$ are the mass-flow averaged temperature at the inlet and outlet of the hot fluid (K), respectively and $T_{in,cold}$ and $T_{out,cold}$ are the are the mass-flow averaged temperature at the inlet and outlet of the cold fluid (K), respectively.

As illustrated by Fig. 21, the benchmark case has up to 18.64% and 12.65% higher overall thermal resistance compared to the optimized and simplified HX units in the laminar region, respectively. This confirms the aforementioned physical interpretations and elucidates that the optimal allocation of the low/moderate

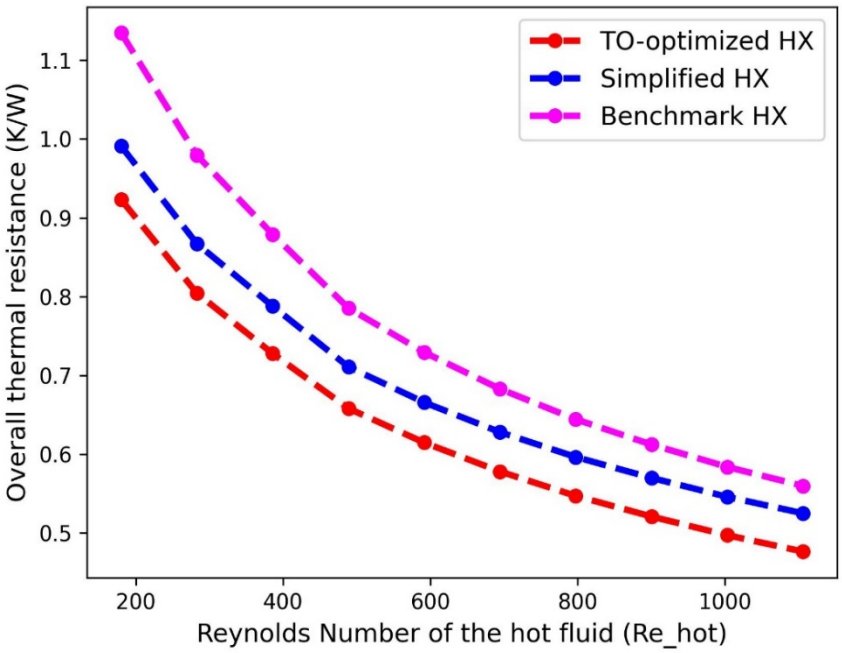

conductive solids for maximized thermo-hydraulic performance is the distant positioning of the interface wall.

Figure 21: Variation of the overall thermal resistance with respect to the Reynolds number for all HXs.

More specifically, when comparing the conduction resistance between the three heat exchangers, defined as the ratio of the average thickness of the HX's middle plate to the solid conduction, multiplied by the heat transfer area, the benchmark HX unit exhibits a higher conduction resistance (0.157 $K \cdot W^{-1}$) compared to both the optimized (0.061 $K \cdot W^{-1}$) and simplified (0.061 $K \cdot W^{-1}$) HX units, which is more than twice as high. Moreover, by comparing the convection thermal resistance of the cold fluid at $\overline{Re_{hot}}$= 695, which is the reciprocal of the product between heat transfer area and the heat transfer coefficient, the optimized HX unit has the lowest convection resistance (0.298 $K.W^{-1}$) compared to the benchmark (0.302 $K.W^{-1}$) and simplified (0,324 $K.W^{-1}$) HX units. Apparently, the difference in convection resistances among the three HX units is negligible when compared to the conduction resistances. This elucidates that the thermal conduction resistance plays a more significant role than the convection resistances in determining the overall thermal resistance, as reflected in the results presented in Figure 21.

Besides, the Biot number that delineates the importance of the fluid's convective heat transfer over the conduction heat transfer inside the solid is assessed for the three HX units as follows:

$$Bi = \frac{h_{hot} D_h}{k_s} \tag{23}$$

where k_s is the thermal conductivity of the SS ($W.m^{-1}.K^{-1}$) and h_{hot} is the convective heat transfer coefficient of the hot fluid ($W.m^{-2}.K^{-1}$) computed using Eq. 24:

$$h_{hot} = \frac{Q_{hot}}{A_{hot}(\overline{T_{hot}} - T_{i,hot})} \tag{24}$$

where Q_{hot} is the heat transfer rate calculated on the hot flow side (W), A_{hot} is the heat transfer area on the hot flow side (m^2), $\overline{T_{hot}}$ is the mass-flow averaged temperature in the hot flow channel (K) and $T_{i,hot}$ is the area-weighted average temperature at the interface wall (interface wall between the hot fluid and the HX's middle plate) of the hot channel (K). As outlined by the Figure 22, the Biot number is higher for the optimized and simplified HX units compared to the benchmark case with an augmentation up to 52.75% and 41.66%, respectively. This underscores the ability of the optimized and simplified designs in intensifying the convective heat transfer of the HXs.

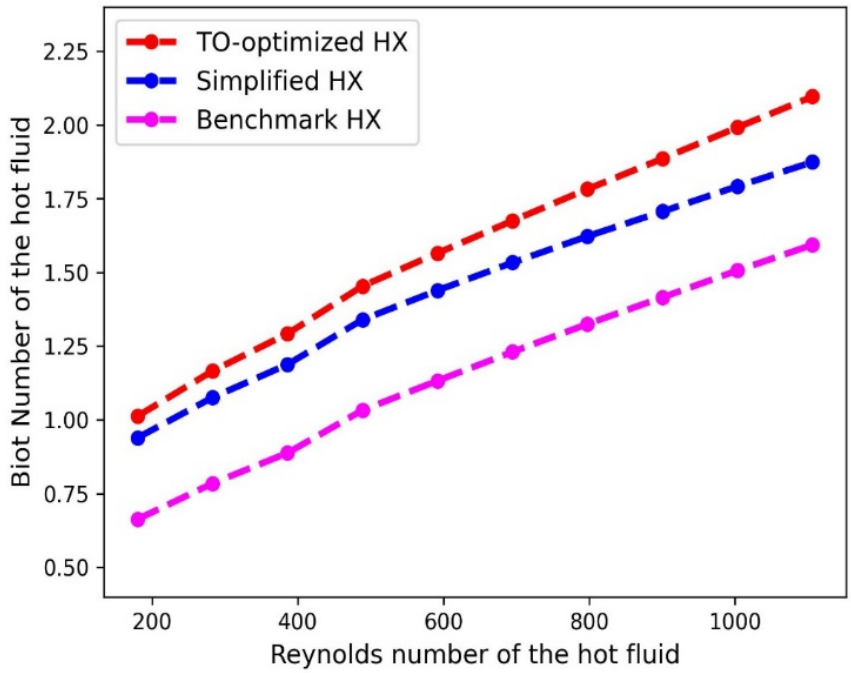

Figure 22: Variation of the Biot number with respect to the Reynolds number for all HX units

6. Conclusions and perspectives

In this article, the density-based TO is conducted on a 2D counter-flow HX unit of moderate conducive material (SS) with narrow design domains for the purpose of maximizing heat transfer rate. An in-depth investigation is carried out to test the effect of different TO's input parameters on the derived topology, showing the sensitivity of the TO's results on the setting input parameters. Despite such impact, it has been revealed that the TO-optimized topology is mainly featured by the allocation of the

moderately conductive solid fins near the insulation walls and not at the HX's interface wall (where heat is exchanged).

In order conduct a comparative analysis with the TO-optimized design, two HX units with rectangular fins are introduced: one having identical solid allocation of the TO-derived design and is named Simplified HX unit and the other have opposite solid allocation and is assigned to the benchmark HX unit. CFD analysis with experimental approaches were adopted to validate the TO's design methodology. The numerical and experimental results show a good agreement between each other both at the global and local levels, demonstrating the thermo-hydraulic performance superiority of the TO-optimized and simplified HX units over the benchmark case with an increase of the exchanged heat up to 15% and 8.7 %, under the same pumping power. This confirms that the distinct manner of fins allocation proposed by the TO, on the enhancement of heat transfer rate of this dual-flow HX unit, particularly when low/moderate conductive material is employed. Eventually, a physical interpretation is delivered to interpret the physics behind the TO-derived design. The positioning of the solids near the insulated wall (as in the TO-derived and simplified designs) aims to locally increase the fluid velocity near the HX's middle plate (where heat is exchanged), leading to a prevailing convective heat transfer over conductive heat transfer, and a reduction in the thermal resistances of the TO-optimized and simplified HX units up to 18.64% and 12.65% compared to the benchmark case, respectively.

The present study focuses on the 2D density-based TO of dual-flow HXs in the laminar flow regime. A potential direction for future research is to extend the current density-based TO approach to 3D industrial heat exchangers operating in the turbulent flow regime. Furthermore, an additional future direction could involve extending the methodology of the present work to address phase change phenomena and incorporate fluid compressibility.

Acknowledgements

This work is financially supported by Région Pays de la Loire within the NExT2Talents program TOP-OPTIM project (998UMR6607 EOTP NEXINTERTALENTHUA).

Declaration of interests

The authors declare that they have no known competing financial interests or personal relationships that could have appeared to influence the work reported in this paper.

Credit authorship contribution statement

Ahmad Fawaz: Writing review & editing, writing original draft, Visualization, Validation, Software, Methodology, Investigation, Formal analysis, **Yuchao Hua:** Writing review & editing, validation, Supervision, Investigation, Formal analysis, Funding. **Steven Le Corre**: Writing review & editing, validation, Supervision, Investigation, Formal analysis. **Yilin Fan:** Writing review & editing, validation, Supervision, Investigation, Formal analysis. **Lingai Luo:** Writing review & editing, Validation, Supervision, Investigation, Formal analysis, Funding, Conceptualization. **Gwenaël Biotteau:** Investigation.

References

[1] Q. Li et al., 'Compact heat exchangers: A review and future applications for a new generation of high temperature solar receivers', *Renewable and Sustainable Energy Reviews*, vol. 15, no. 9, pp. 4855–4875, Dec. 2011 [Online]. Available: 10.1016/j.rser.2011.07.066.

[2] L. Luo et al., 'Design, Fabrication And Experimental Study Of New Compact Mini Heat-Exchangers', in *Microreaction Technology*, M. Matlosz, W. Ehrfeld, and J. P. Baselt, Eds. Berlin, Heidelberg: Springer Berlin Heidelberg, 2001, pp. 68–69[Online]. Availablehttp://link.springer.com/10.1007/978-3-642-56763-6_7[Accessed: 12January2022].

[3] L. Luo et al., 'Heat exchanger: from micro- to multi-scale design optimization', *Int. J. Energy Res.*, vol. 31, no. 13, pp. 1266–1274, Oct. 2007 [Online]. Available: 10.1002/er.1298.

[4] O. P. Arsenyeva et al., 'Optimal design of plate-and-frame heat exchangers for efficient heat recovery in process industries', *Energy*, vol. 36, no. 8, pp. 4588–4598, Aug. 2011 [Online]. Available: 10.1016/j.energy.2011.03.022.

[5] H. Jouhara et al., 'Experimental and theoretical investigation of a flat heat pipe heat exchanger for waste heat recovery in the steel industry', *Energy*, vol. 141, pp. 1928–1939, Dec. 2017 [Online]. Available: 10.1016/j.energy.2017.10.142.

[6] H. Jouhara et al., 'Investigation on a full-scale heat pipe heat exchanger in the ceramics industry for waste heat recovery', *Energy*, vol. 223, p. 120037, May 2021 [Online]. Available: 10.1016/j.energy.2021.120037.

[7] P. Pongsoi et al., 'Heat transfer and flow characteristics of spiral fin-and-tube heat exchangers: A review', *International Journal of Heat and Mass Transfer*, vol. 79, pp. 417–431, Dec. 2014 [Online]. Available: 10.1016/j.ijheatmasstransfer.2014.07.072.

[8] B. Sahin and A. Demir, 'Performance analysis of a heat exchanger having perforated square fins', *Applied Thermal Engineering*, vol. 28, no. 5–6, pp. 621–632, Apr. 2008 [Online]. Available: 10.1016/j.applthermaleng.2007.04.003.

[9] M.-Y. Wen and C.-Y. Ho, 'Heat-transfer enhancement in fin-and-tube heat exchanger with improved fin design', *Applied Thermal Engineering*, vol. 29, no. 5–6, pp. 1050–1057, Apr. 2009 [Online]. Available: 10.1016/j.applthermaleng.2008.05.019.

[10] L. H. Tang et al., 'Experimental and numerical investigation on air-side performance of fin-and-tube heat exchangers with various fin patterns', *Experimental Thermal and Fluid Science*, vol. 33, no. 5, pp. 818–827, Jul. 2009 [Online]. Available: 10.1016/j.expthermflusci.2009.02.008.

[11] A. Maji and G. Choubey, 'Improvement of heat transfer through fins: A brief review of recent developments', *Heat Trans*, vol. 49, no. 3, pp. 1658–1685, May 2020 [Online]. Available: 10.1002/htj.21684.

[12] A. Fawaz et al., 'Topology optimization of heat exchangers: A review', *Energy*, p. 124053, Apr. 2022 [Online]. Available: 10.1016/j.energy.2022.124053.

[13] R. Boichot and L. Luo, 'A simple Cellular Automaton algorithm to optimise heat transfer in complex configurations', *International Journal of Exergy*, vol. 7, pp. 51–64, 2010.

[14] Y. Du et al., 'Size optimization of heat exchanger and thermoeconomic assessment for supercritical CO2 recompression Brayton cycle applied in marine', *Energy*, vol. 239, p. 122306, Jan. 2022 [Online]. Available: 10.1016/j.energy.2021.122306.

[15] Y. Li et al., 'Tailoring the fluid flow distribution in a parallel mini-channel heat sink under multiple-peak heat flux', *Thermal Science and Engineering Progress*, vol. 29, p. 101182, Mar. 2022 [Online]. Available: 10.1016/j.tsep.2021.101182.

[16] Y. Hua et al., 'Machine-learning topology optimization with stochastic gradient descent optimizer for heat conduction problems', *International Journal of Heat and Mass Transfer*, vol. 223, p. 125226, May 2024 [Online]. Available: 10.1016/j.ijheatmasstransfer.2024.125226.

[17] Q. Wang et al., 'Enhancing plate-fin heat exchanger hydraulic thermal performance through air-side fin optimization based on pseudo-3D topology optimization', *Applied Thermal Engineering*, vol. 252, p. 123642, Sep. 2024 [Online]. Available: 10.1016/j.applthermaleng.2024.123642.

[18] Q. Yang et al., 'Multi-layer topology optimization of dual-fluid convective heat transfer in printed circuit heat exchangers', *Applied Thermal Engineering*, vol. 257, p. 124434, Dec. 2024 [Online]. Available: 10.1016/j.applthermaleng.2024.124434.

[19] W. Xuan et al., 'Numerical simulation and thermodynamic test analysis of plate heat exchanger based on topology optimization', *Applied Thermal Engineering*, vol. 255, p. 123882, Oct. 2024 [Online]. Available: 10.1016/j.applthermaleng.2024.123882.

[20] Y. Li et al., 'Numerical and experimental investigation of optimized heat sink designs for liquid cooling of a heterogeneous heating surface with multiple heat sources', *International Journal of Thermal Sciences*, vol. 209, p. 109540, Mar. 2025 [Online]. Available: 10.1016/j.ijthermalsci.2024.109540.

[21] C. Yang et al., 'Topology optimization of rectangular parallel plate heat exchanger unit', *International Journal of Thermal Sciences*, vol. 208, p. 109503, Feb. 2025 [Online]. Available: 10.1016/j.ijthermalsci.2024.109503.

[22] Y. Li et al., 'Design and Optimization of Heat Sinks for the Liquid Cooling of Electronics with Multiple Heat Sources: A Literature Review', *Energies*, vol. 16, no. 22, p. 7468, Nov. 2023 [Online]. Available: 10.3390/en16227468.

[23] Y. Li et al., 'A genetic algorithm-based topology optimization (GATO) method for convective cooling of a heating surface with multiple heat sources', *International Journal of Heat and Mass Transfer*, vol. 224, p. 125349, Jun. 2024 [Online]. Available: 10.1016/j.ijheatmasstransfer.2024.125349.

[24] X. Han et al., 'Topology optimization for spider web heat sinks for electronic cooling', *Applied Thermal Engineering*, vol. 195, p. 117154, Aug. 2021 [Online]. Available: 10.1016/j.applthermaleng.2021.117154.

[25] P. Papazoglou, 'Topology Optimization of Heat Exchangers', Master's thesis, Delft University of Technology, 2015.

[26] R. Tawk et al., 'Topology optimization of heat and mass transfer problems in two fluids—one solid domains', *Numerical Heat Transfer, Part B: Fundamentals*, vol. 76, no. 3, pp. 130–151, Sep. 2019 [Online]. Available: 10.1080/10407790.2019.1644919.

[27] H. Kobayashi et al., 'Topology design of two-fluid heat exchange', *Struct Multidisc Optim*, vol. 63, no. 2, pp. 821–834, Feb. 2021 [Online]. Available: 10.1007/s00158-020-

02736-8.

[28] J. H. K. Haertel et al., 'Topology optimization of a pseudo 3D thermofluid heat sink model', *International Journal of Heat and Mass Transfer*, vol. 121, pp. 1073–1088, Jun. 2018 [Online]. Available: 10.1016/j.ijheatmasstransfer.2018.01.078.

[29] T. Kondoh et al., 'Drag minimization and lift maximization in laminar flows via topology optimization employing simple objective function expressions based on body force integration', *Struct Multidisc Optim*, vol. 45, no. 5, pp. 693–701, May 2012 [Online]. Available: 10.1007/s00158-011-0730-z.

[30] C. F. Hvejsel and E. Lund, 'Material interpolation schemes for unified topology and multi-material optimization', *Struct Multidisc Optim*, vol. 43, no. 6, pp. 811–825, Jun. 2011 [Online]. Available: 10.1007/s00158-011-0625-z.

[31] J. Alexandersen et al., 'Topology optimisation for natural convection problems: TOPOLOGY OPTIMISATION FOR NATURAL CONVECTION PROBLEMS', *Int. J. Numer. Meth. Fluids*, vol. 76, no. 10, pp. 699–721, Dec. 2014 [Online]. Available: 10.1002/fld.3954.

[32] O. Sigmund and J. Petersson, 'Numerical instabilities in topology optimization: A survey on procedures dealing with checkerboards, mesh-dependencies and local minima', *Structural Optimization*, vol. 16, no. 1, pp. 68–75, Aug. 1998 [Online]. Available: 10.1007/BF01214002.

[33] B. S. Lazarov and O. Sigmund, 'Filters in topology optimization based on Helmholtz-type differential equations', *Int. J. Numer. Meth. Engng.*, vol. 86, no. 6, pp. 765–781, May 2011 [Online]. Available: 10.1002/nme.3072.

[34] F. Wang et al., 'On projection methods, convergence and robust formulations in topology optimization', *Struct Multidisc Optim*, vol. 43, no. 6, pp. 767–784, Jun. 2011 [Online]. Available: 10.1007/s00158-010-0602-y.

[35] K. Thulukkanam, *Heat Exchanger Design Handbook*, 0 ed. CRC Press, 2013[Online]. Availablehttps://www.taylorfrancis.com/books/9781439842133[Accessed: 12February2023].

[36] C. Zillober, 'A globally convergent version of the method of moving asymptotes', *Structural Optimization*, vol. 6, no. 3, pp. 166–174, Sep. 1993 [Online]. Available: 10.1007/BF01743509.

[37] J. Alexandersen et al., 'Large scale three-dimensional topology optimisation of heat sinks cooled by natural convection', *International Journal of Heat and Mass Transfer*, vol. 100, pp. 876–891, Sep. 2016 [Online]. Available: 10.1016/j.ijheatmasstransfer.2016.05.013.

[38] F. A. S. Mota et al., 'Modeling and Design of Plate Heat Exchanger', in *Heat Transfer Studies and Applications*, M. S. N. Kazi, Ed. InTech, 2015[Online]. Availablehttp://www.intechopen.com/books/heat-transfer-studies-and-applications/modeling-and-design-of-plate-heat-exchanger[Accessed: 3May2022].

[39] H. Kobayashi et al., 'Freeform winglet design of fin-and-tube heat exchangers guided by topology optimization', *Applied Thermal Engineering*, vol. 161, p. 114020, Oct. 2019 [Online]. Available: 10.1016/j.applthermaleng.2019.114020.

[40] X. Han et al., 'Topology optimization for spider web heat sinks for electronic cooling', *Applied Thermal Engineering*, vol. 195, p. 117154, Aug. 2021 [Online]. Available: 10.1016/j.applthermaleng.2021.117154.

[41] P. E. Gill et al., 'SNOPT: An SQP Algorithm for Large-Scale Constrained Optimization', *SIAM Rev.*, vol. 47, no. 1, pp. 99–131, Jan. 2005 [Online]. Available: 10.1137/S0036144504446096.

[42] A. Wächter and L. T. Biegler, 'On the implementation of an interior-point filter line-search algorithm for large-scale nonlinear programming', *Math. Program.*, vol. 106, no. 1, pp. 25–57, Mar. 2006 [Online]. Available: 10.1007/s10107-004-0559-y.

[43] Y. Hua et al., 'Heat Spreading Effect on the Optimal Geometries of Cooling Structures in A Manifold Heat Sink'. 2023[Online]. Availablehttps://www.ssrn.com/abstract=4625528[Accessed: 8July2024].

[44] S. B. Dilgen et al., 'Density based topology optimization of turbulent flow heat transfer systems', *Struct Multidisc Optim*, vol. 57, no. 5, pp. 1905–1918, May 2018 [Online]. Available: 10.1007/s00158-018-1967-6.

[45] F. R. Menter, 'Two-equation eddy-viscosity turbulence models for engineering applications', *AIAA Journal*, vol. 32, no. 8, pp. 1598–1605, Aug. 1994 [Online]. Available: 10.2514/3.12149.

[46] S. Yun et al., 'Numerical analysis on thermo-fluid–structural performance of graded lattice channels produced by metal additive manufacturing', *Applied Thermal Engineering*, vol. 193, p. 117024, Jul. 2021 [Online]. Available: 10.1016/j.applthermaleng.2021.117024.

[47] D. Liang et al., 'Investigating the effect of element shape of the face-centered cubic lattice structure on the flow and endwall heat transfer characteristics in a rectangular channel', *International Journal of Heat and Mass Transfer*, vol. 153, p. 119579, Jun. 2020 [Online]. Available: 10.1016/j.ijheatmasstransfer.2020.119579.

[48] S. Yun et al., 'Heat transfer and stress characteristics of additive manufactured FCCZ lattice channel using thermal fluid-structure interaction model', *International Journal of Heat and Mass Transfer*, vol. 149, p. 119187, Mar. 2020 [Online]. Available: 10.1016/j.ijheatmasstransfer.2019.119187.

[49] N. H. Naqiuddin et al., 'Numerical investigation for optimizing segmented micro-channel heat sink by Taguchi-Grey method', *Applied Energy*, vol. 222, pp. 437–450, Jul. 2018 [Online]. Available: 10.1016/j.apenergy.2018.03.186.

[50] I. B. Celik et al., 'Procedure for Estimation and Reporting of Uncertainty Due to Discretization in CFD Applications', *J. Fluids Eng.*, vol. 130, no. 7, p. 078001, 2008 [Online]. Available: 10.1115/1.2960953.

[51] T. Astarita and G. M. Carlomagno, *Infrared Thermography for Thermo-Fluid-Dynamics*. Berlin, Heidelberg: Springer Berlin Heidelberg, 2013[Online]. Availablehttps://link.springer.com/10.1007/978-3-642-29508-9[Accessed: 29April2024].

[52] 'Crystan Ltd, Sapphire (Al2O3), Crystan Ltd (2019).' [Online]. Availablehttps://www.crystran.co.uk/optical-materials/sapphire-al2o3.

[53] K. E. Kaylegian et al., 'Influence of fatty acid chain length and unsaturation on mid-infrared milk analysis', *Journal of Dairy Science*, vol. 92, no. 6, pp. 2485–2501, Jun. 2009 [Online]. Available: 10.3168/jds.2008-1910.

[54] R. J. Moffat, 'Describing the uncertainties in experimental results', *Experimental Thermal and Fluid Science*, vol. 1, no. 1, pp. 3–17, Jan. 1988 [Online]. Available: 10.1016/0894-

1777(88)90043-X.